

## STARRY: ANALYTICAL OCCULTATION LIGHT CURVES

RODRIGO LUGER,<sup>1</sup> ERIC AGOL,<sup>2</sup> JAVID LUSTIG-FLEMING,<sup>1</sup> RUSSELL DEITRICK,<sup>3</sup> AND DANIEL FOREMAN-MACKEY<sup>4</sup>

<sup>1</sup>*Department of Astronomy, University of Washington, Seattle, WA*

<sup>2</sup>*Department of Astronomy, University of Washington, Seattle, WA; Virtual Planetary Laboratory;  
Guggenheim Fellow*

<sup>3</sup>*Center for Space and Habitability, University of Bern, Bern, Switzerland*

<sup>4</sup>*Center for Computational Astrophysics, Flatiron Institute, New York, NY*

### ABSTRACT

We derive analytical, closed form solutions for the total flux received from a spherical planet, moon or star during an occultation if the specific intensity map of the body is expressed as a sum of spherical harmonics. Our expressions are valid to arbitrary degree and may be computed recursively for speed. The formalism we develop here applies to the computation of stellar transit light curves, planetary secondary eclipse light curves, and planet-planet/planet-moon occultation light curves, as well as thermal (rotational) phase curves. We present **starry**, an open-source photodynamical code written in C++ and wrapped in Python that computes these light curves. **starry** also computes analytical derivatives of the light curves with respect to all input parameters for use in gradient-based inference schemes such as Hamiltonian monte carlo (HMC), allowing users to quickly and efficiently regress on observed light curves to infer properties of a celestial body's surface map.

*Keywords:* methods: analytical — techniques: photometric

## 1. INTRODUCTION

Our understanding of the surface of Earth and the other planets in our solar system starts with the creation of maps. Mapping the colors, compositions, and surface features gives us an understanding of the geological, hydrological, and meteorological processes at play that are the basis of planetary science, including comparative planetology. With the discovery of planets orbiting other stars, map-making becomes a formidable task: these planets are too distant to resolve their surfaces into maps as we do for our own planetary suite. One way to overcome this drawback is to utilize the time-dependence of unresolved, disk-integrated light from planetary bodies: both rotational variability and occultations yield the opportunity to constrain the presence of static variations in the surface features of exoplanets.

The first application of time-dependent mapping to exoplanets was carried out in the infrared with the hot Jupiter HD 189733b using both phase-variations and secondary eclipses of the exoplanet (Knutson et al. 2007; Majeau et al. 2012; de Wit et al. 2012). These yielded crude constraints on the monopole and dipole components of the thermal emission from the thick, windy atmosphere of this giant planet. The subsequent discovery of vast numbers of smaller planets has opened the possibility of applying the mapping technique to exoplanets with solid or liquid surfaces (e.g., Cowan et al. 2012, 2013; Cowan & Fujii 2017; Fujii et al. 2017; Luger et al. 2017).

- Phase curves are a subset of rotational light curves when a planet is tidally locked.
- Cite Pál (2012) and mention Green’s theorem.
- Discuss JWST and prospects for exocartography.
- Mention other relevant papers.
- ...



This paper is organized as follows: in §2 we discuss the real spherical harmonics and introduce our mathematical formalism for dealing with spherical harmonic surface maps. In §3 we discuss how to compute analytical phase curves and occultation light curves for these surface maps. In §4 we introduce our photodynamical code, `starry`, and discuss how to use it to compute full light curves for systems of exoplanets and other celestial bodies. We present important caveats in §5 and conclude in §6. Most of the math, including the derivations of the analytic expressions for the light curves, is folded into the Appendix. For convenience, throughout the paper we provide links to Python code ( ) to reproduce all of the figures, as well as links to Mathematica (Wolfram Research, Inc. 2016) scripts and PDFs ( ) containing proofs and derivations of the principal equations. Finally, Table 1 at the end lists all the symbols used in the paper, with references to the equations defining them.

## 2. SURFACE MAPS

### 2.1. Spherical harmonics

The orthonormalized real spherical harmonics  $Y_{lm}(\theta, \phi)$  of degree  $l \geq 0$  and order  $m \in [-l, l]$  with the Condon-Shortley phase factor (e.g. Varshalovich et al. 1988) are defined in spherical coordinates as

$$Y_{lm}(\theta, \phi) = \begin{cases} \bar{P}_{lm}(\cos \theta) \cos(m\phi) & m \geq 0 \\ \bar{P}_{l|m|}(\cos \theta) \sin(|m|\phi) & m < 0, \end{cases} \quad (1)$$

where  $\bar{P}_{lm}$  are the normalized associated Legendre functions (Equation A2). On the surface of the unit sphere, we have

$$\begin{aligned} x &= \sin \theta \cos \phi \\ y &= \sin \theta \sin \phi \\ z &= \cos \theta. \end{aligned} \quad (2)$$

The observer is located along the  $z$ -axis at  $z = \infty$  such that the projected disk of the body sits at the origin on the  $xy$ -plane with  $\hat{\mathbf{x}}$  to the right and  $\hat{\mathbf{y}}$  up. Re-writing Equation (1) in terms of  $x$ ,  $y$ , and  $z$  leads to expressions that are simply polynomials of these variables, a fact we will heavily exploit below when computing their integrals. We derive the polynomimal representation of the spherical harmonics in Appendix A. The spherical harmonics up to degree  $l = 5$  are shown in Figure 1.

### 2.2. Surface map vectors

Any physical surface map of a celestial body can be expanded in terms of the real spherical harmonics defined in the previous section. For convenience, in this paper we represent a surface map as a vector  $\mathbf{y}$  of spherical harmonic coefficients such that the specific intensity at the point  $(x, y)$  may be written

$$I(x, y) = \tilde{\mathbf{y}}^T(x, y) \mathbf{y}, \quad (3)$$

where  $\tilde{\mathbf{y}}$  is the *spherical harmonic basis*, arranged in increasing degree and order:

$$\tilde{\mathbf{y}} = \left( Y_{0,0} \ Y_{1,-1} \ Y_{1,0} \ Y_{1,1} \ Y_{2,-2} \ Y_{2,-1} \ Y_{2,0} \ Y_{2,1} \ Y_{2,2} \ \dots \right)^T, \quad (4)$$

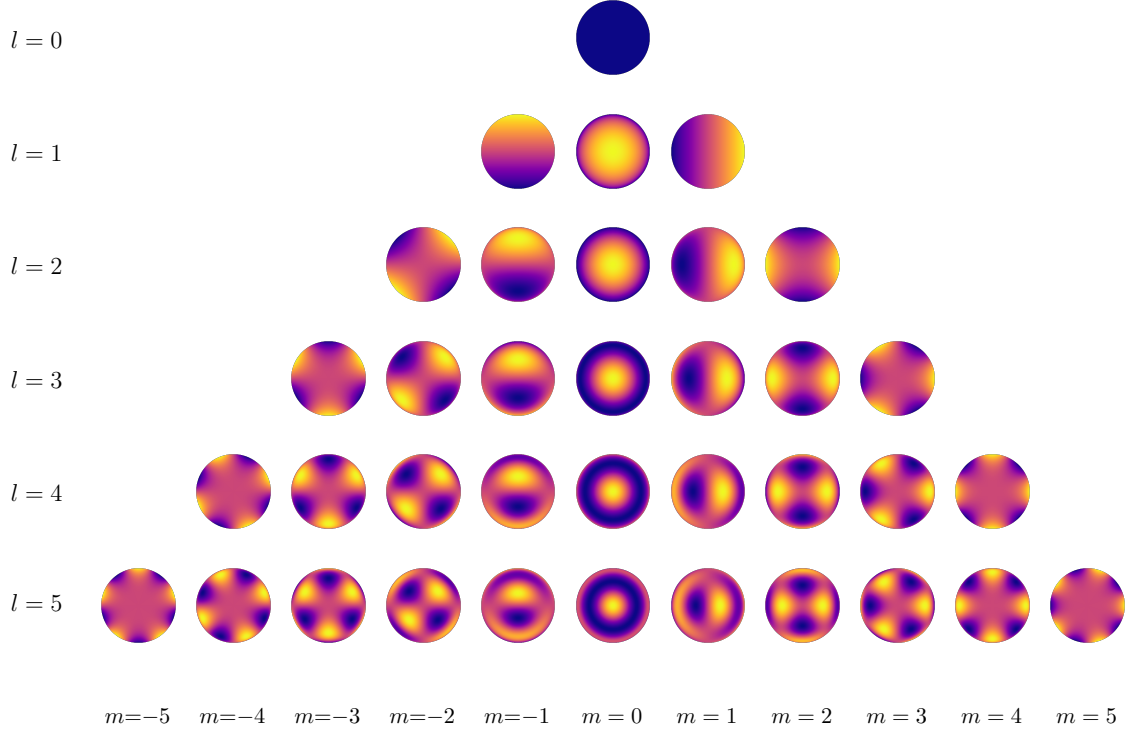


**Figure 1.** The real spherical harmonics up to degree  $l = 5$  computed from Equation (1). In these plots, the  $x$ -axis points to the right, the  $y$ -axis points up, and the  $z$ -axis points out of the page. Click on the link on the right to view an animated version.



where  $Y_{l,m} = Y_{l,m}(x, y)$  are given by Equation (A9). For reference, in this basis the coefficient of the spherical harmonic  $Y_{l,m}$  is located at the index

$$n = l^2 + l + m \quad (5)$$

of the vector  $\mathbf{y}$ . Conversely, the coefficient at index  $n$  of  $\mathbf{y}$  corresponds to the spherical harmonic of degree and order given by

$$\begin{aligned} l &= \lfloor \sqrt{n} \rfloor \\ m &= n - \lfloor \sqrt{n} \rfloor^2 - \lfloor \sqrt{n} \rfloor. \end{aligned} \quad (6)$$

### 2.3. Change of basis

In order to compute the occultation light curve for a body with a given surface map  $\mathbf{y}$ , it is convenient to first find its polynomial representation  $\mathbf{p}$ , which we express

as a vector of coefficients in the *polynomial basis*  $\tilde{\mathbf{p}}$ :

$$\tilde{p}_n = \begin{cases} x^{\frac{\mu}{2}} y^{\frac{\nu}{2}} & \nu \text{ even} \\ x^{\frac{\mu-1}{2}} y^{\frac{\nu-1}{2}} z & \nu \text{ odd} \end{cases}$$

$$\tilde{\mathbf{p}} = \left( 1 \ x \ z \ y \ x^2 \ xz \ xy \ yz \ y^2 \ \dots \right)^T, \quad (7)$$


where

$$\begin{aligned} \mu &= l - m \\ \nu &= l + m \end{aligned} \quad (8)$$

with  $l$  and  $m$  given by Equation (6). To find  $\mathbf{p}$  given  $\mathbf{y}$ , we introduce the change of basis matrix  $\mathbf{A}_1$ , which transforms a vector in the spherical harmonic basis  $\tilde{\mathbf{y}}$  to the polynomial basis  $\tilde{\mathbf{p}}$ :

$$\mathbf{p} = \mathbf{A}_1 \mathbf{y} \quad (9)$$

The columns of  $\mathbf{A}_1$  are simply the polynomial vectors corresponding to each of the spherical harmonics in Equation (4); see Appendix B for details. As before, the specific intensity at the point  $(x, y)$  may be computed as

$$\begin{aligned} I(x, y) &= \tilde{\mathbf{p}}^T \mathbf{p} \\ &= \tilde{\mathbf{p}}^T \mathbf{A}_1 \mathbf{y}. \end{aligned} \quad (10)$$

As we will see in the next section, integrating the surface map over the disk of the body is easier if we apply one final transformation to our input vector, rotating it into

what we will refer to as the *Green's basis*,  $\tilde{\mathbf{g}}$ :

$$\tilde{g}_n = \begin{cases} \frac{\mu+2}{2} x^{\frac{\mu}{2}} y^{\frac{\nu}{2}} & \nu \text{ even} \\ z & l=1, m=0 \\ 3x^{l-2}yz & \nu \text{ odd, } \mu=1, l \text{ even} \\ z \left( -x^{l-3} + x^{l-1} + 4x^{l-3}y^2 \right) & \nu \text{ odd, } \mu=1, l \text{ odd} \\ z \left( \frac{\mu-3}{2} x^{\frac{\mu-5}{2}} y^{\frac{\nu-1}{2}} - \frac{\mu-3}{2} x^{\frac{\mu-5}{2}} y^{\frac{\nu+3}{2}} - \frac{\mu+3}{2} x^{\frac{\mu-1}{2}} y^{\frac{\nu-1}{2}} \right) & \text{otherwise} \end{cases}$$

$$\tilde{\mathbf{g}} = \left( 1 \ 2x \ z \ y \ 3x^2 \ -3xz \ 2xy \ 3yz \ y^2 \ \dots \right)^T, \quad (11)$$


where the values of  $l$ ,  $m$ ,  $\mu$ , and  $\nu$  are given by Equations (6) and (8). Given a polynomial vector  $\mathbf{p}$ , the corresponding vector in the Green's basis,  $\mathbf{g}$ , can be found by performing another change of basis operation:

$$\mathbf{g} = \mathbf{A}_2 \mathbf{p} \quad (12)$$

where the columns of the matrix  $\mathbf{A}_2$  are the Green's vectors corresponding to each of the polynomial terms in Equation (7); see Appendix B for details.

Note that we may also transform directly from the spherical harmonic basis to the Green's basis:

$$\begin{aligned} \mathbf{g} &= \mathbf{A}_2 \mathbf{A}_1 \mathbf{y} \\ &= \mathbf{A} \mathbf{y} \end{aligned} \quad (13)$$

where

$$\mathbf{A} \equiv \mathbf{A}_2 \mathbf{A}_1 \quad (14)$$

is the full change of basis matrix. For completeness, we again note that the specific intensity at a point on a map described by the spherical harmonic vector  $\mathbf{y}$  may be

written

$$\begin{aligned} I(x, y) &= \tilde{\mathbf{g}}^T(x, y)\mathbf{g} \\ &= \tilde{\mathbf{g}}^T(x, y)\mathbf{A}\mathbf{y}. \end{aligned} \quad (15)$$

#### 2.4. Rotation of surface maps

Defining a map as a vector of spherical harmonic coefficients makes it straightforward to compute the projection of the map under arbitrary rotations of the body via a rotation matrix  $\mathbf{R}$ :

$$\mathbf{y}' = \mathbf{R}\mathbf{y} \quad (16)$$

where  $\mathbf{y}'$  are the spherical harmonic coefficients of the rotated map. In Appendix C we derive expressions for  $\mathbf{R}$  in terms of the Euler angles  $\alpha$ ,  $\beta$ , and  $\gamma$ , as well as in terms of an angle  $\theta$  and an arbitrary axis of rotation  $\mathbf{u}$ . Follow the link next to Figure 1 to view an animation of the spherical harmonics rotating about the  $y$ -axis, computed from Equation (16).

### 3. COMPUTING LIGHT CURVES

#### 3.1. Rotational phase curves

Consider a body of unit radius centered at the origin, with a surface map given by the spherical harmonic vector  $\mathbf{y}$  viewed at an orientation specified by the rotation matrix  $\mathbf{R}$ , such that the specific intensity at a point  $(x, y)$  on the surface is

$$\begin{aligned} I(x, y) &= \tilde{\mathbf{y}}^T(x, y)\mathbf{R}\mathbf{y} \\ &= \tilde{\mathbf{p}}^T(x, y)\mathbf{A}_1\mathbf{R}\mathbf{y} \end{aligned} \quad (17)$$

where  $\tilde{\mathbf{p}}$  is the polynomial basis and  $\mathbf{A}_1$  is the corresponding change-of-basis matrix (§2.3). The total flux radiated in the direction of the observer is obtained by integrating the specific intensity over a region  $S$  of the projected disk of the body:

$$\begin{aligned} F &= \iint I(x, y) dS \\ &= \iint \tilde{\mathbf{p}}^T(x, y)\mathbf{A}_1\mathbf{R}\mathbf{y} dS \\ &= \mathbf{r}^T\mathbf{A}_1\mathbf{R}\mathbf{y}, \end{aligned} \quad (18)$$

where  $\mathbf{r}$  is a column vector whose  $n^{\text{th}}$  component is given by

$$r_n \equiv \iint \tilde{p}_n(x, y) dS. \quad (19)$$

When the entire disk of the body is visible (i.e., when no occultation is occurring), this may be written

$$r_n = \int_{-1}^1 \int_{-\sqrt{1-x^2}}^{\sqrt{1+x^2}} \tilde{p}_n(x, y) dy dx$$

$$= \begin{cases} \frac{\Gamma\left(\frac{\mu}{4} + \frac{1}{2}\right) \Gamma\left(\frac{\nu}{4} + \frac{1}{2}\right)}{\Gamma\left(\frac{\mu+\nu}{4} + 2\right)} & \frac{\mu}{2} \text{ even, } \frac{\nu}{2} \text{ even} \\ \frac{\sqrt{\pi}}{2} \frac{\Gamma\left(\frac{\mu}{4} + \frac{1}{4}\right) \Gamma\left(\frac{\nu}{4} + \frac{1}{4}\right)}{\Gamma\left(\frac{\mu+\nu}{4} + 2\right)} & \frac{\mu-1}{2} \text{ even, } \frac{\nu-1}{2} \text{ even} \\ 0 & \text{otherwise.} \end{cases} \quad (20)$$


where  $\Gamma(\cdot)$  is the gamma function. Equation (18) may be used to analytically compute the rotational phase curve of a body with an arbitrary surface map. Since  $\mathbf{r}$  and  $\mathbf{A}_1$  are independent of the map coefficients or its orientation, these may be pre-computed for computational efficiency.

### 3.2. Occultation light curves

As we showed earlier, the specific intensity at a point  $(x, y)$  on the surface of a body described by the map  $\mathbf{y}$  and the rotation matrix  $\vec{R}$  may also be written as

$$\begin{aligned} I(x, y) &= \tilde{\mathbf{y}}^\top(x, y) \mathbf{R} \mathbf{y} \\ &= \tilde{\mathbf{g}}^\top(x, y) \mathbf{A} \mathbf{R} \mathbf{y}, \end{aligned} \quad (21)$$

where  $\tilde{\mathbf{g}}$  is the Greens basis and  $\mathbf{A}$  is the full change of basis matrix (§2.3). As before, the total flux radiated in the direction of the observer is obtained by integrating the specific intensity over a region  $S$  of the projected disk of the body:

$$\begin{aligned} F &= \iint I(x, y) dS \\ &= \iint \tilde{\mathbf{g}}^\top(x, y) \mathbf{A} \mathbf{R} \mathbf{y} dS \\ &= \mathbf{s}^\top \mathbf{A} \mathbf{R} \mathbf{y}, \end{aligned} \quad (22)$$

where  $\mathbf{s}$  is a column vector whose  $n^{\text{th}}$  component is given by

$$s_n \equiv \iint \tilde{g}_n(x, y) dS. \quad (23)$$

This time, suppose the body is occulted by another body of radius  $r$  centered at the point  $(x_o, y_o)$ , so that the surface  $S$  over which the integral is taken is a function of  $r$ ,  $x_o$ , and  $y_o$ . In general, the integrals in Equation (23) are difficult (and often impossible) to compute directly. One way to simplify the problem is to first perform a rotation through an angle

$$\omega = \frac{\pi}{2} - \arctan 2(y_o, x_o) \quad (24)$$

about the  $z$ -axis ( $\mathbf{u} = [0, 0, 1]$ ) so that the occultor lies along the  $+y$ -axis, with its center located a distance  $b = \sqrt{x_o^2 + y_o^2}$  from the origin (see Figure 2). In this rotated frame, the limits of integration (the two points of intersection between the occultor and the occulted body, should they exist) are symmetric about the  $y$ -axis. If we define  $\phi \in [-\pi/2, \pi/2]$  as the angular position of the right hand side intersection point relative to the occultor center, measured counter-clockwise from the  $+x$  direction, the arc of the occultor that overlaps the occulted body extends from  $\pi - \phi$  to  $2\pi + \phi$  (see the Figure). Similarly, defining  $\lambda \in [-\pi/2, \pi/2]$  as the angular position of the same point relative to the origin, the arc of the portion of the occulted body that is visible during the occultation extends from  $\pi - \lambda$  to  $2\pi + \lambda$  (see the Figure). For future reference, it can be shown that

$$\phi = \begin{cases} \arcsin\left(\frac{1 - r^2 - b^2}{2br}\right) & |1 - r| < b < 1 + r \\ \frac{\pi}{2} & b \leq 1 - r \end{cases} \quad (25)$$


and

$$\lambda = \begin{cases} \arcsin\left(\frac{1 - r^2 + b^2}{2b}\right) & |1 - r| < b < 1 + r \\ \frac{\pi}{2} & b \leq 1 - r, \end{cases} \quad (26)$$


The case  $b \leq 1 - r$  corresponds to an occultation during which the occultor is fully within the planet disk, so no points of intersection exist. In this case, we define  $\phi$  such that the arc from  $\pi - \phi$  to  $2\pi + \phi$  spans the entire circumference of the occultor, and  $\lambda$  such that the arc from  $\pi - \lambda$  to  $2\pi + \lambda$  spans the entire circumference of the occulted body. Note that if  $b \geq 1 + r$ , no occultation occurs and the flux may be

computed as in §3.1, while if  $b \leq r - 1$ , the entire disk of the body is occulted and the total flux is zero.

The second trick we employ to solve Equation (30) is to use Green's theorem to express the surface integral of  $\tilde{\mathbf{g}}_n$  as the line integral of a vector function  $\mathbf{G}_n$  along the boundary of the same surface (Pál 2012):

$$s_n = \iint \tilde{g}_n(x, y) dS = \oint \mathbf{G}_n(x, y) \cdot d\mathbf{r} \quad (27)$$

where  $\mathbf{G}_n(x, y) = G_{nx}(x, y)\hat{\mathbf{x}} + G_{ny}(x, y)\hat{\mathbf{y}}$  is chosen such that

$$\mathbf{D} \wedge \mathbf{G}_n = \tilde{g}_n(x, y). \quad (28)$$

The operation  $\mathbf{D} \wedge \mathbf{G}_n$  denotes the *exterior derivative* of  $\mathbf{G}_n$ . In two-dimensional Cartesian coordinates, it is given by

$$\mathbf{D} \wedge \mathbf{G}_n \equiv \frac{dG_{ny}}{dx} - \frac{dG_{nx}}{dy}. \quad (29)$$

Thus, in order to compute  $s_n$  in Equation (27), we must (1) apply a rotation to our map  $\mathbf{y}$  to align the occultor with the  $+y$ -axis; (2) find a vector function  $\mathbf{G}_n$  whose exterior derivative is the  $n^{\text{th}}$  component of the vector basis  $\tilde{\mathbf{g}}$  (Equation 11); and (3) integrate it along the boundary of the visible portion of the occulted body's surface. In general, for an occultation involving two bodies, this boundary consists of two arcs: a segment of the circle bounding the occultor (thick red curve in Figure 2), and a segment of the circle bounding the occulted body (thick black curve in Figure 2). If we happen to know  $\mathbf{G}_n$ , the integral in Equation (27) is just

$$s_n = \mathcal{Q}(\mathbf{G}_n) - \mathcal{P}(\mathbf{G}_n), \quad (30)$$

where, as in Pál (2012), we define the *primitive integrals*

$$\mathcal{P}(\mathbf{G}_n) = \int_{\pi-\phi}^{2\pi+\phi} [G_{ny}(rc_\varphi, b + rs_\varphi)c_\varphi - G_{nx}(rc_\varphi, b + rs_\varphi)s_\varphi] r d\varphi \quad (31)$$

and

$$\mathcal{Q}(\mathbf{G}_n) = \int_{\pi-\lambda}^{2\pi+\lambda} [G_{ny}(c_\varphi, s_\varphi)c_\varphi - G_{nx}(c_\varphi, s_\varphi)s_\varphi] d\varphi, \quad (32)$$

where, as before,  $c_\varphi \equiv \cos \varphi$  and  $s_\varphi \equiv \sin \varphi$  and we used the fact that along the arc of a circle,

$$d\mathbf{r} = -rs_\varphi d\varphi \hat{\mathbf{x}} + rc_\varphi d\varphi \hat{\mathbf{y}}. \quad (33)$$

In Equations (31) and (32),  $\mathcal{P}(\mathbf{G}_n)$  is the line integral along the arc of the occultor and  $\mathcal{Q}(\mathbf{G}_n)$  is the line integral along the arc of the occulted body.

As cumbersome as the Green's basis (Equation 11) may appear, the reason we introduced it is that its anti-exterior derivatives are conveniently simple. It can be easily shown that one possible solution to Equation (28) is

$$\mathbf{G}_n(x, y) = \begin{cases} x^{\frac{\mu+2}{2}} y^{\frac{\nu}{2}} \hat{\mathbf{y}} & \nu \text{ even} \\ \frac{1-z^3}{3(1-z^2)} (-y \hat{\mathbf{x}} + x \hat{\mathbf{y}}) & l=1, m=0 \\ x^{l-2} z^3 \hat{\mathbf{x}} & \nu \text{ odd}, \mu=1, l \text{ even} \\ x^{l-3} y z^3 \hat{\mathbf{x}} & \nu \text{ odd}, \mu=1, l \text{ odd} \\ x^{\frac{\mu-3}{2}} y^{\frac{\nu-1}{2}} z^3 \hat{\mathbf{y}} & \text{otherwise,} \end{cases} \quad (34)$$


where  $l$  and  $m$  are given by Equation (6) and  $\mu$  and  $\nu$  are given by Equation (8). Solving the occultation problem is therefore a matter of evaluating the primitive integrals of  $\mathbf{G}_n$  (Equations 31 and 32). The solutions are in general tedious, but they are all analytical, involving sines, cosines, and complete elliptic integrals. In Appendix D we derive recurrence relations to quickly compute these. We note, in particular, that the solutions all involve complete elliptic integrals of the *same* argument, so that the elliptic integrals need only be evaluated once for a map of arbitrary degree, greatly improving the evaluation speed and the scalability of the problem to high order.

### 3.3. Summary

Here we briefly summarize how to analytically compute the flux during an occultation of a body whose specific intensity profile is described by a sum of spherical harmonics. Given a body of unit radius with a surface map described by the vector of spherical harmonic coefficients  $\mathbf{y}$  (Equation 4), occulted by another body of radius  $r$  centered at the point  $(x_o, y_o)$ , we must:

1. Compute the rotation matrix  $\mathbf{R}$  to rotate the map to the correct viewing orientation, which may be specified by the Euler angles  $\alpha$ ,  $\beta$ , and  $\gamma$  (Appendix C.1) or by an axis  $\mathbf{u}$  and an angle  $\theta$  (Appendix C.2).

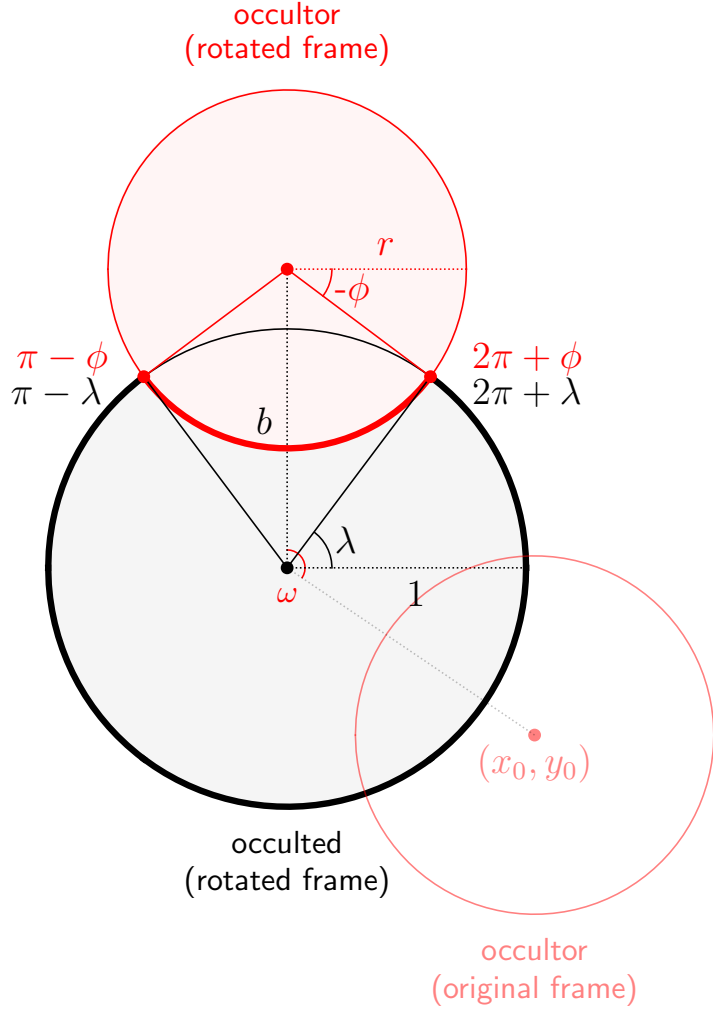


**Figure 2.** Geometry of the occultation problem. The occulted body is centered at the origin and has unit radius, while the occultor is centered at  $(x_o, y_o)$  and has radius  $r$ . We first rotate the two bodies about the origin through an angle  $\theta = \pi/2 - \arctan2(y_o, x_o)$  so the problem is symmetric about the  $y$ -axis. In this frame, the occultor is located at  $(0, b)$ , where  $b = \sqrt{x_o^2 + y_o^2}$  is the impact parameter. The arc of the occultor that overlaps the occulted body (thick red curve) now extends from  $\pi - \phi$  to  $2\pi + \phi$ , measured from the center of the occultor. The arc of the occulted body that is visible during the occultation (thick black curve) extends from  $\pi - \lambda$  to  $2\pi + \lambda$ , measured from the origin. These are the curves along which the primitive integrals (Equations 31 and 32) are evaluated. The angles  $\phi$  and  $\lambda$  are given by Equations (25) and (26) and extend from  $-\pi/2$  to  $\pi/2$ . When the occultor is completely within the disk of the occulted body, we define  $\phi = \lambda = \pi/2$ .

&lt;/&gt;

2. Compute the rotation matrix  $\mathbf{R}'$  to rotate the map by an angle  $\omega$  about the  $+z$ -axis (Equation 24) so the center of the occultor is a distance  $b = \sqrt{x_o^2 + y_o^2}$  along the  $+y$ -axis from the center of the occulted body.
3. Compute the change-of-basis matrix  $\mathbf{A}$  (§2.3) to convert our vector of spherical harmonic coefficients to a vector of polynomial coefficients in the Green's basis (Equation 11). Since  $\mathbf{A}$  is the same for all occultations, this matrix may be pre-computed to improve computational speed.
4. Compute the solution vector  $\mathbf{s}$  (Equation 30), with  $\mathcal{P}(\mathbf{G}_n)$  and  $\mathcal{Q}(\mathbf{G}_n)$  given by Equations (D32) and (D33) in the Appendix. Note that  $s_2$  is special and must be computed separately (Equation D21).

Given these quantities, the total flux during an occultation is then just

$$F = \mathbf{s}^T \mathbf{A} \mathbf{R}' \mathbf{R} \mathbf{y} . \quad (35)$$

#### 4. THE STARRY CODE PACKAGE

The `starry` code package provides code to analytically compute light curves for celestial bodies using the formalism developed in this paper. `starry` is coded entirely in C++ for speed and wrapped in Python using `pybind11` (Jakob et al. 2017) for quick and easy light curve calculations. The code may be installed by running the following in a terminal:

```
1 git clone https://github.com/rodluger/starry.git
2 cd starry
3 python setup.py develop
```

There are two primary ways of interfacing with `starry`: via the surface map class `starry.Map` and via the celestial body system class `starry.System`. The former gives users the most flexibility to create and manipulate surface maps and compute their fluxes for a variety of applications, while the latter provides a quick and easy (but limited) way to generate light curves for exoplanet systems. Let us discuss the map class first.

##### 4.1. Creating a map

To begin using `starry`, execute the following in a Python environment:

```
1 from starry import Map
```

A `starry Map` is a vector of spherical harmonic coefficients, indexed by increasing degree and order, as in Equation (4). We can create a map of spherical harmonics up to degree  $l_{\max} = 5$  by typing

```
2 m = Map(5)
```

By default, all coefficients are set to zero. Say our surface map is given by the function

$$I(x, y) = -2Y_{5,-3}(x, y) + 2Y_{5,0}(x, y) + Y_{5,4}(x, y). \quad (36)$$

To instantiate this map, we set the corresponding coefficients in `m`:

```
3 m[5, -3] = -2
4 m[5, 0] = 2
5 m[5, 4] = 1
```

Printing the map to screen yields

```
<STARRY Map: -2 Y_{5,-3} + 2 Y_{5,0} + Y_{5,4}>
```

Users can also directly access the spherical harmonic vector `y`, polynomial vector `p`, and Green's polynomial vector `g` via the attributes `m.y`, `m.p`, and `m.g`, respectively:

```
# m.y
[0, 0, 0, 0, 0, 0, 0, 0, 0, 0, 0, 0, 0, 0, 0, 0, 0, 0, 0, 0,
 0, 0, 0, 0, 0, 0, 0, -2, 0, 0, 2, 0, 0, 0, 0, 1, 0]

# m.p
[0, 0, 1.87, 0, 0, 0, 0, 0, 0, 0, -13.10, -23.48, 0, 0,
 -13.10, 7.83, 0, 0, 0, 0, 0, 0, 0, 0, 16.81, 26.42,
 0, 0, 17.02, 17.61, 0, 0, 16.81, -8.81]

# m.g
[0, 0, 0, 0, 0, 0, 0, 0, 0, 0, 3.73, -7.83, 0, 0, 1.86,
 7.83, 0, 0, 0, 0, 0, 0, 0, 0, -5.59, 5.28, 0, 0,
 -16.81, 5.87, 0, 0, -16.75, -8.81])
```

Once a map is instantiated, users may quickly visualize it by calling

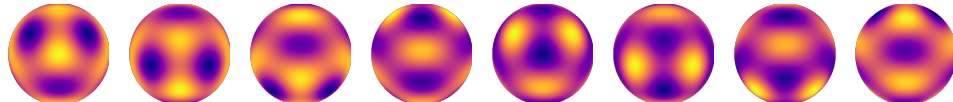
```
14 m.show()
```

or

```
15 m.animate(u=u)
```

where `u` defines the axis of rotation for the animation. Rotation of this map about  $\hat{x}$  yields

</>



Alternatively, users may provide the path to an image file of the surface map on a rectangular latitude-longitude grid or a ring-ordered Healpix<sup>1</sup> map array:

<sup>1</sup> <http://healpix.sf.net>

```
16 m.load_image("/path/to/image.jpg")
```

or

```
17 m.load_healpix(array)
```

In both cases, `starry` uses the `map2alm()` function of the `healpy` package to find the expansion of the map in terms of spherical harmonics. Keep in mind that if the image contains very dark pixels (with RGB values close to zero), its spherical harmonic expansion may lead to regions with *negative* specific intensity, which is of course unphysical.

In Figure 3 we show a simplified two-color map of the cloudless Earth and its corresponding `starry` instance for  $l_{\max} = 10$ , rotated successively about  $\hat{\mathbf{y}}$ .

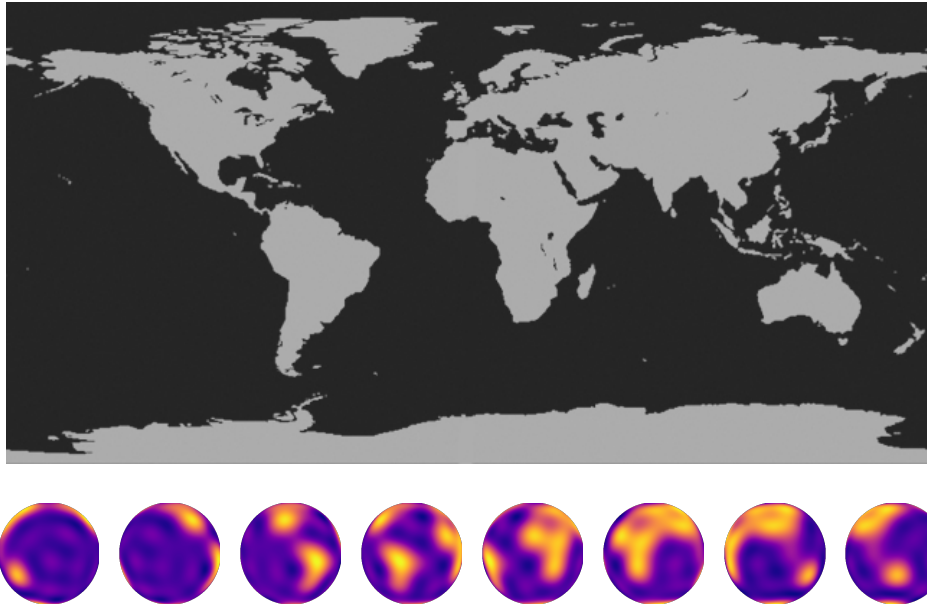


**Figure 3.** A simplified two-color map of the cloudless Earth (top) and the corresponding tenth-degree spherical harmonic expansion, rotated about  $\hat{\mathbf{y}}$  (bottom).



#### 4.2. Computing rotational phase curves

Once a map is instantiated, it is easy to compute its rotational phase curve, `F`:

```
18 F = m.flux(u=u, theta=theta)
```

where `u` is the axis of rotation and `theta` is an array of angles (in radians) for which to compute the flux. Note that rotations performed by `flux()` are not cumulative; instead, all angles should be specified relative to the original, unrotated map frame. In the top panel of Figure 4 we plot rotational phase curves for all spherical harmonics up to  $l_{\max} = 6$  for rotation about  $\hat{\mathbf{x}}$  (blue curves) and  $\hat{\mathbf{y}}$  (orange curves). The small dots correspond to phase curves computed by numerical evaluation of the flux on an

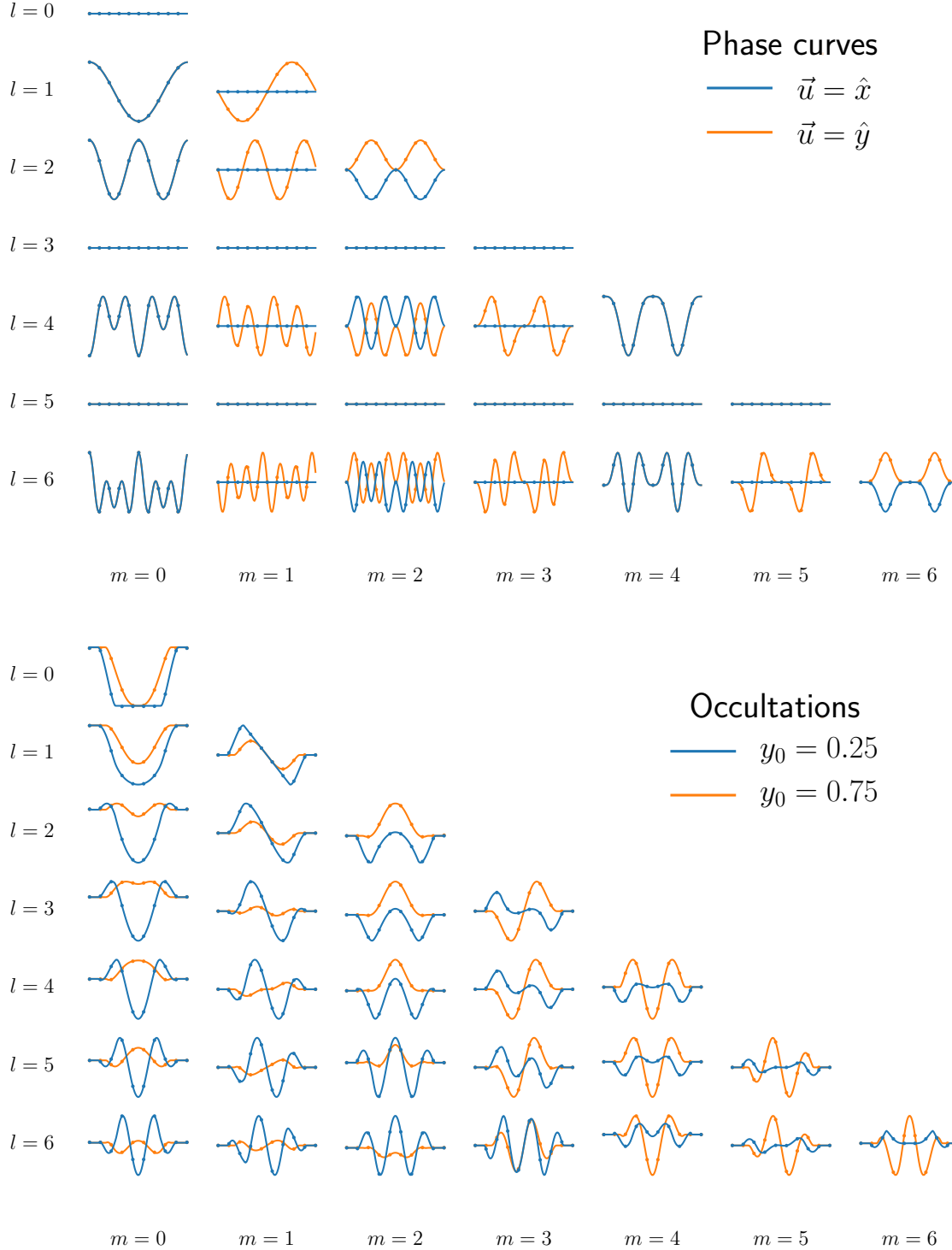


**Figure 4.** *Top:* Phase curves for the first several spherical harmonics with order  $m \geq 0$  rotated about the  $x$ -axis (blue) and about the  $y$ -axis (orange). Odd harmonics with  $l > 1$  and harmonics with  $m < 0$  are in the phase curve null space (Cowan et al. 2013). *Bottom:* Occultation light curves for the same set of spherical harmonics. An occultor of radius  $r = 0.3$  transits the body along the  $+x$  direction at  $y_0 = 0.25$  (blue) and  $y_0 = 0.75$  (orange).

</>  
</>

adaptive radial mesh (see §4.7). As discussed by Cowan et al. (2013), harmonics with odd  $l > 1$  and those with  $m < 0$  (not plotted) are in the null space and therefore do not exhibit rotational phase variations.

As a second example, we can compute the rotational phase curve of the simplified Earth model (Figure 3) for rotation about  $\hat{\mathbf{y}}$  (its actual spin axis) by executing

```
19 theta = np.linspace(0, 2 * np.pi, 100)
20 F = m.flux(u=[0, 1, 0], theta=theta)
```

The variable  $F$  is an array of flux values computed from Equation (18); we plot this in Figure 5, alongside the rotational phase curves due to each of the seven individual continents.

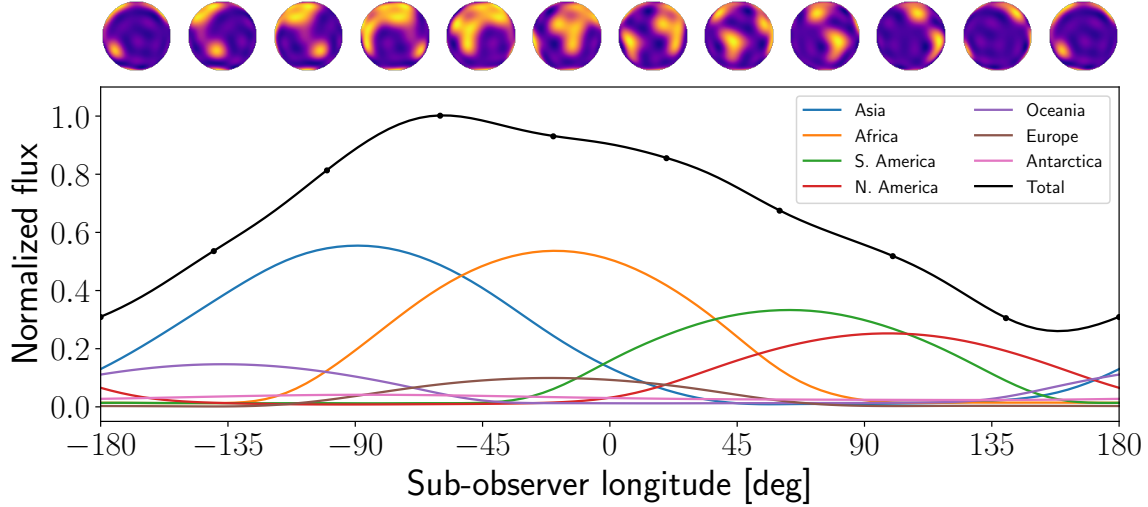


**Figure 5.** Phase curve for the Earth rotating about its axis, computed from the  $l_{\max} = 10$  expansion from Figure 3. The full rotational phase curve is shown in black, and the flux due to each of the seven continents is shown as the colored curves (see legend). The black dots correspond to the numerical solution.

&lt;/&gt;

#### 4.3. Computing occultation light curves

Occultation light curves are similarly easy to compute:

```
21 F = m.flux(u=u, theta=theta, xo=xo, yo=yo, ro=ro)
```

where  $u$  and  $\theta$  are the same as above, and  $x_0$ ,  $y_0$ , and  $r_0$  are the occultor parameters ( $x$  position,  $y$  position, and radius, all in units of the occulted body's radius), which may be either scalars or arrays.

In the bottom panel of Figure 4 we plot occultation light curves for the spherical harmonics with  $m \geq 0$  up to  $l_{\max} = 6$ . The occultor has radius  $r = 0.3$  and moves at a constant speed along the  $x$  direction at  $y_o = 0.25$  (blue curves) and  $y_o = 0.75$  (orange curves). The light curve of any body undergoing such an occultation can be expressed as a weighted sum of these light curves. Note that because the value of

individual spherical harmonics can be negative, an increase in the flux is visible at certain points during the occultation; however, this would of course not occur for any physical map constructed from a linear combination of the spherical harmonics. Note also that unlike in the case of rotational phase curves, there is no null space for occultations, as all spherical harmonics (including those with  $m < 0$ , which are not shown) produce a flux signal during occultation. As before, the numerical solutions are shown as the small dots.

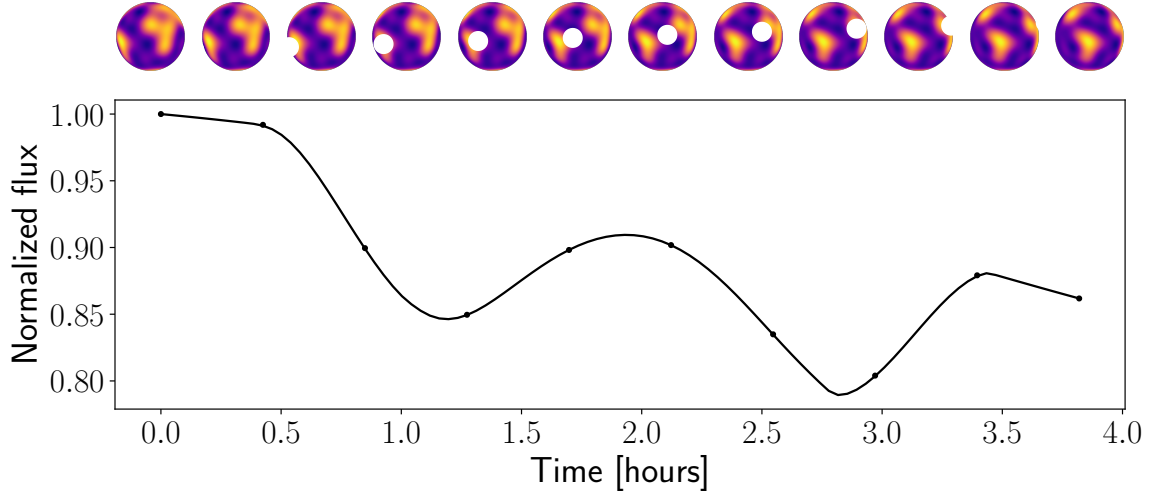


**Figure 6.** Occultation light curve for the Moon transiting the rotating Earth, computed from the  $l_{\max} = 10$  expansion from Figure 3. The two largest dips are due to the occultations of South America (left) and Africa (right). Once again, the black dots correspond to the numerical solution.

&lt;/&gt;

To further illustrate the code, we return to our spherical harmonic expansion of the Earth. Figure 6 shows an occultation light curve computed for a hypothetical transit of the Earth by the Moon. The occultation lasts about four hours, during which time the sub-observer point rotates from Africa to South America, causing a steady flux decrease as the Pacific Ocean rotates into view. The occultation is double-dipped: one dip due to the occultation of South America, and one dip due to the occultation of Africa.

#### 4.4. Computing transit light curves

The formalism developed in this paper can easily be extended to the case of occultations (transits) of limb-darkened stars by noting that any radially symmetric specific intensity profile can be expressed as a sum over the  $m = 0$  spherical harmonics (see Figure 1). In particular, Luger & Agol (2018) show how a limb darkening profile that is an order  $l$  polynomial function of the radial coordinate,  $\mu = z = \sqrt{1 - x^2 - y^2}$ , can be exactly expressed in terms of the  $m = 0$  spherical harmonics up to order  $l$ .

For convenience, we implement this functionality in `starry`, allowing users to specify the coefficients of the limb darkening polynomial directly as follows:

```
22 m = Map(2)
23 m.set_ld(1) = u1
24 m.set_ld(2) = u2
```

or, more compactly,<sup>2</sup>

```
25 m[1] = u1
26 m[2] = u2
```

In either case, this sets the map's limb darkening profile to

$$I(\mu)/I_0 = 1 - u_1(1 - \mu) - u_2(1 - \mu)^2, \quad (37)$$

with  $\mu$  given above, corresponding to the well-known case of a quadratically limb-darkened star. From Luger & Agol (2018), this corresponds to the spherical harmonic sum

$$I(x, y) = \frac{2\sqrt{\pi}}{3}(3 - 3u_1 + 4u_2)Y_{0,0} + \frac{2\sqrt{\pi}}{\sqrt{3}}(u_1 + 2u_2)Y_{1,0} - \frac{4\sqrt{\pi}}{3\sqrt{5}}u_2Y_{2,0}. \quad (38)$$


Note, importantly, that setting the limb darkening coefficients of a map resets all  $m \neq 0$  coefficients. `starry` does not at present support adding limb darkening to pre-existing, non-radially symmetric maps; this functionality will be added in the future to allow for limb darkening of, say, planetary atmospheres.

Figure 7 shows a transit light curve computed with `starry` for  $u_1 = 0.4, u_2 = 0.26$ . The planet/star radius ratio is  $r = 0.1$  and the planet transits at impact parameter  $b = 0.5$ . For comparison, we also compute the flux with `batman` (Kreidberg 2015) and with a high precision numerical integration of the surface integral of Equation (37). The error on the transit depth for `starry` flux is less than  $10^{-5}$  parts per million everywhere in the light curve.

#### 4.5. Photodynamics

The `starry.Map` class discussed above is convenient when the rotational state of the body in question and/or the position of the occultor is known, or when these can easily be computed by some other means. For convenience, `starry` implements a simple Keplerian solver to compute stellar and planetary light curves for exoplanet systems given the orbital parameters as input. Users can access this functionality by instantiating a `starry.Star` and any number of `starry.Planet` objects, then passing them to a `starry.System` instance. Let us begin by creating a star:

```
27 from starry import Star
28 star = Star(lmax=2)
```

<sup>2</sup> Note that when two indices are used to access the map vector, as in §4.1, `starry` interprets them as the  $l$  and  $m$  spherical harmonic indices. When a single index is used, as in this case, `starry` interprets it as the limb darkening polynomial index.

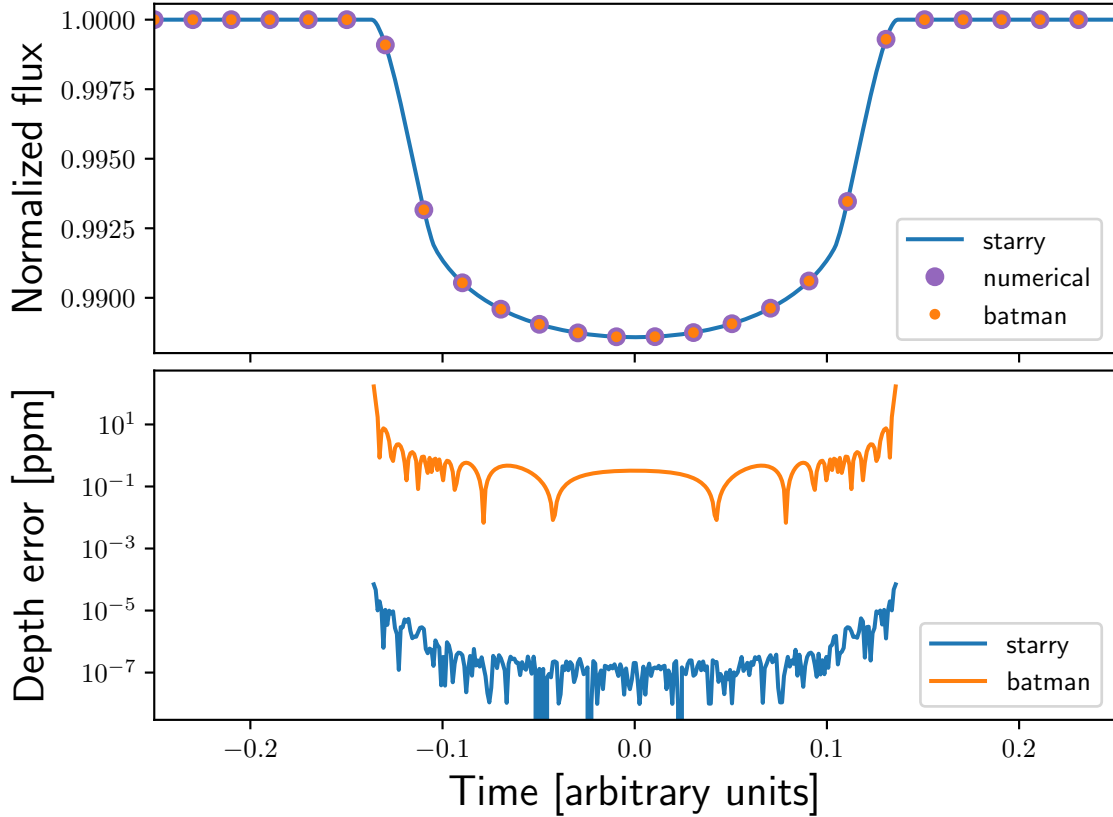


**Figure 7.** Sample transit light curve for a planet ( $r = 0.1$ ) transiting a quadratically limb-darkened star ( $u_1 = 0.4, u_2 = 0.26$ ). The top panel shows the `starry` (blue curve) and `batman` (orange dots) light curves, as well as a light curve generated by a high precision direct numerical integration of the surface integral (purple dots). The bottom panel shows the fractional error on the transit depth in parts per million relative to the numerical solution for `starry` (blue) and `batman` (orange).

&lt;/&gt;

A `starry.Star` has unit radius and unit luminosity; the planet's radii, semi-major axes, and luminosities are all defined relative to these. By default, the star's map is set to the constant ( $Y_{0,0}$ ) term, corresponding to uniform surface brightness. We can add quadratic limb darkening as before by editing the star's `map` attribute:

```
29 star.map[1] = 0.40
30 star.map[2] = 0.26
```

where we arbitrarily set  $u_1 = 0.40$  and  $u_2 = 0.26$ . Next, we can instantiate a planet by typing

```
31 from starry import Planet
32 planet = Planet(lmax=1, r=0.1, L=5.e-3, porb=4.3, prot=4.3)
```

where `lmax` is the highest degree of the planet map, `r` is the planet radius in units of the stellar radius, `L` is the total planet luminosity in units of the stellar luminosity, `porb` is the orbital period and `prot` is the rotational period, both in days. Several other keyword

arguments may be provided; these are detailed in full in the [documentation](#). As with `starry.Star`, the planet's map can be accessed via the `map` property. Suppose we wish to give the planet a simple dipole map ( $Y_{1,0}$ ) with peak brightness at the sub-stellar point. By default, the planet is instantiated at a transiting configuration (new phase), with mean longitude `lambda0 = 90°`, so we must actually set the corresponding coefficient in the map to be *negative*:

```
33 planet.map[1, 0] = -1
```

This ensures that the hot spot is on the side of the planet facing the star (away from the observer when the planet is transiting). <sup>3</sup>

Finally, care must always be taken to ensure the map is positive everywhere. In our case, this requires that the coefficient of the  $Y_{0,0}$  term be at least  $\sqrt{3}$ : <sup>4</sup>

```
34 planet.map[0, 0] = 1.75
```

For more details on ensuring surface maps are positive everywhere, see §5.

We are now ready to instantiate the planetary system:

```
35 from starry import System
36 system = System([star, planet])
```

(note that the star must always be listed first). We can now compute the full light curve:

```
37 system.compute(time)
```

where `time` is the array of times (in days) at which to compute the light curve. This command internally calls the `flux()` method of each of the surface maps, populating the `flux` attribute of each body with its respective light curve. The total light curve (the sum of the light curves of each of the bodies in the system, including the star) is stored in `system.flux`. The top panel of Figure 8 shows the light curve for the system we instantiated above: both the transits and secondary eclipses of the planet are clearly visible. For flair, we added a hotspot offset of  $15^\circ$  to simulate advection of heat by a westward wind, causing the peak of the planet's phase curve to occur slightly before secondary eclipse (refer to the Python script for details).

The bottom panel of the figure shows a two-planet system with more elaborate surface maps. In addition to the transits, eclipses, and complex phase curve morphology, several planet-planet occultations are also visible in the light curve.

#### 4.6. Gradients of the light curves

We still need to think about how to expose the autodiff stuff to the user.



todo

<sup>3</sup> Alternatively, users may specify the map as seen from full phase and set `planet.lambda0 = 270`.

<sup>4</sup> In Cartesian coordinates, we have  $Y_{0,0} = \sqrt{\frac{1}{4\pi}}$  and  $Y_{1,0} = \sqrt{\frac{3}{4\pi}}z$ . At the anti-stellar point ( $z = 1$ ), the ratio of these two terms is  $\sqrt{3}$ , so the coefficient of  $Y_{0,0}$  must be at least this value to ensure the anti-stellar point has a nonnegative surface intensity.

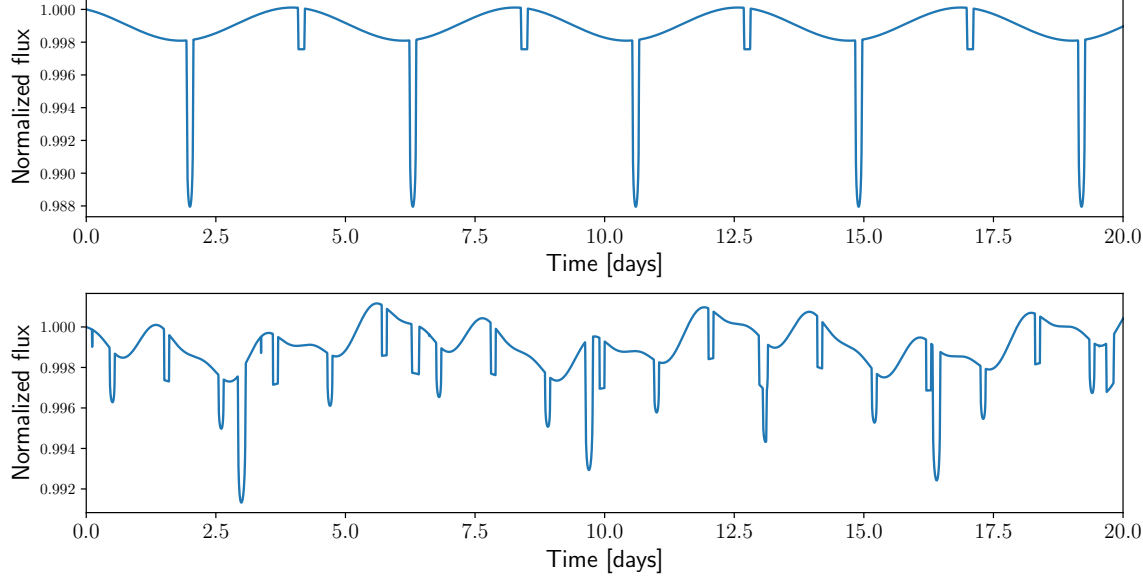


**Figure 8.** Sample analytical exoplanet system light curves computed with `starry`. *Top:* a hot Jupiter transiting a Sun-like star. The planet’s map is a simple dipole, with the hotspot offset  $15^\circ$  from stellar noon; the offset in the secondary eclipse from the peak of the phase curve is apparent. *Bottom:* a two-planet system with more complex surface maps. In addition to transits and secondary eclipses, a few planet-planet occultations are visible (e.g., the very short events at  $t = 0.1$  and  $t = 3.4$  days).



#### 4.7. Benchmarks

We validate all our calculations of rotational phase curves and occultation light curves by comparing them to numerical solutions of the corresponding surface integrals. We integrate the specific intensity of the body by discretely summing over its surface map on an adaptive radial mesh whose resolution is iteratively increased wherever the spatial gradient of the specific intensity is large and in the vicinity of the limb of the occultor. Click on the link at right for an animation of our adaptive mesh scheme.



In `starry`, users can request numerical solutions to the flux by typing

```
38 F = m.flux(u=u, theta=theta, xo=xo, yo=yo, ro=ro,
39     numerical=True, tol=1.e-4)
```

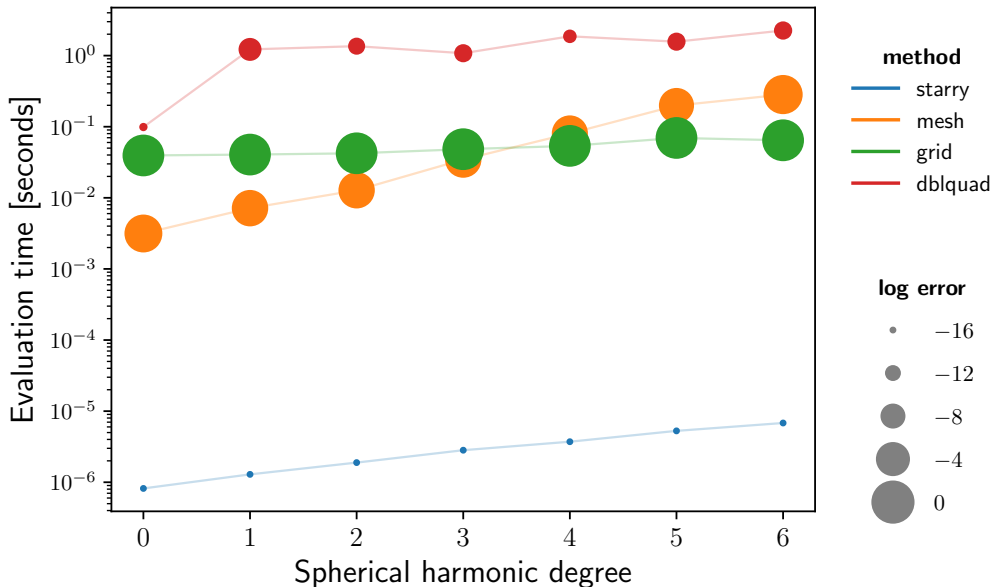
where `tol` is the error tolerance, the maximum absolute value of the difference between the specific intensity at the center of a grid cell to the average of the specific intensity at the four vertices of the same cell. The mesh is locally refined until the requested tolerance is met in all cells.

All light curves in Figure 4 show the flux computed in this way as the small points along each of the curves. We find that our analytical light curves agree with the numerical solutions to within the error of the latter.

#### 4.8. Speed tests

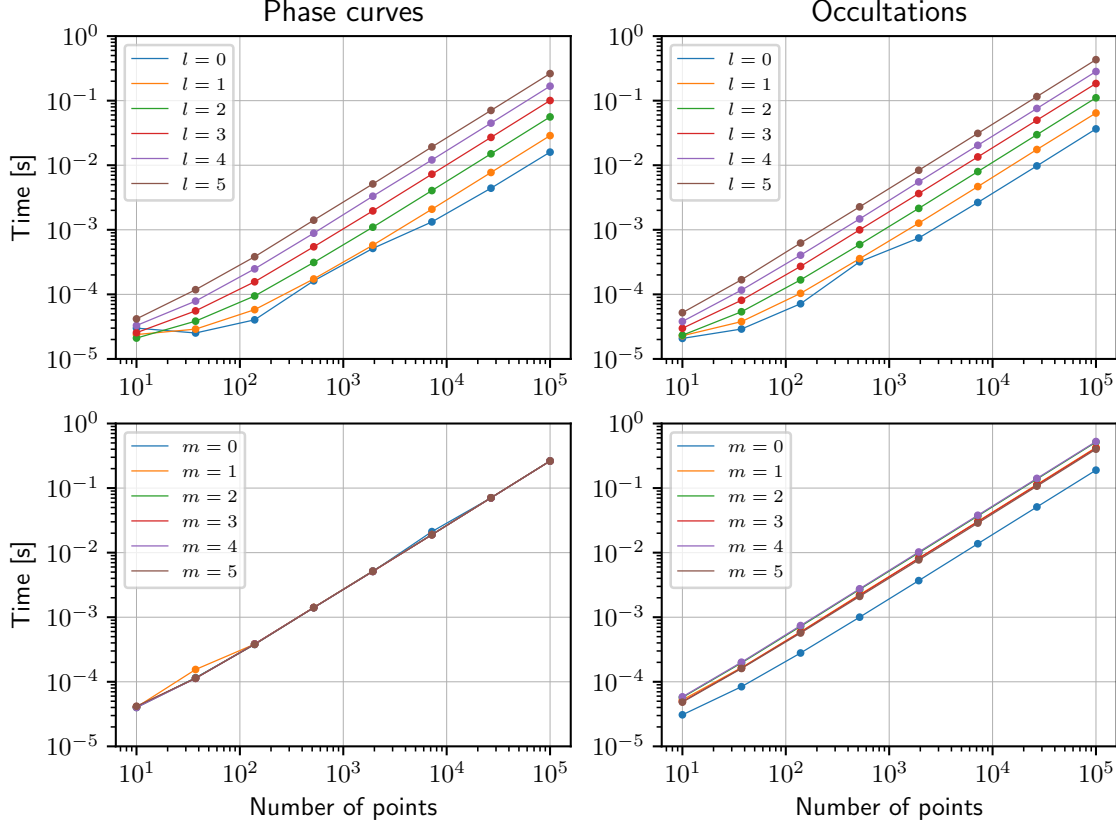
Figure 9 shows the evaluation time for occultation calculations as a function of the spherical harmonic degree  $l$  of the map. Analytical solutions computed with `starry` are shown as the blue dots. Also shown are calculations using the adaptive mesh technique described in the previous section (orange dots), brute-force integration on a  $300 \times 300$  Cartesian grid (green dots), and numerical evaluation of the double integral using the `scipy.integrate dblquad` (Jones et al. 2001) routine (red). The size of each point is proportional to the log of the fractional error relative to the `starry` solution. Light curve computation using `starry` is several orders of magnitude faster and more accurate than any other evaluation technique.

Figure 10 shows the evaluation time for `starry` as a function of the number of points in the light curve for phase curves (left) and occultation light curves (right). The top panel shows curves for maps of different degree  $l$ , and the bottom panel shows curves for single-order maps of degree  $l = 5$ . Evaluation time scales exponentially with increasing degree, but `starry` can compute full occultation light curves for  $l = 5$  maps with  $10^5$  points in under one second. Evaluation time is roughly constant across the different orders at fixed degree, except  $m = 0$ , which is substantially faster to evaluate (blue curve, bottom right). `starry` is therefore particularly efficient at calculating light curves for symmetric maps, such as those of limb-darkened stars. In Figure 11 we show a speed comparison to the `batman` transit package (Kreidberg 2015) for transits across a quadratically limb-darkened star. `starry` is as efficient as `batman` at computing transit light curves.



**Figure 9.** Evaluation time for a single occultation calculation as a function of the spherical harmonic degree of the map using `starry` (blue), the adaptive mesh technique (§4.7, orange), brute force integration on a Cartesian grid (green), and `scipy`'s `dblquad` two-dimensional numerical integration routine (red). The size of each point is proportional to the log of the error relative to the `starry` analytical solution.





**Figure 10.** Speed tests for `starry`, showing the light curve evaluation time as a function of number of light curve points for rotational phase curves (left) and occultation light curves (right) of individual spherical harmonics. The top panels show the evaluation time for spherical harmonics of different degrees  $l$ , averaged over all orders  $m$ . The bottom panels show the evaluation time for each of the positive orders of the  $l = 5$  spherical harmonics. </>

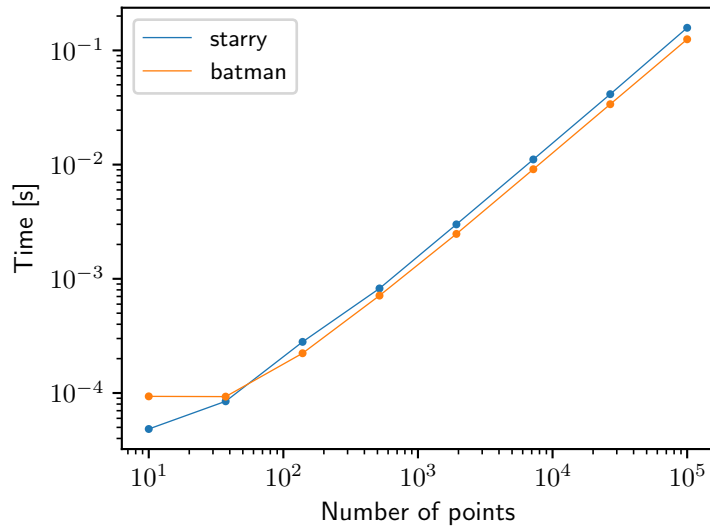


**Figure 11.** Speed comparison to the `batman` transit modeling package (Kreidberg 2015) for a hot Jupiter transit across a quadratically limb-darkened star. </>

## 5. CAVEATS

### 5.1. Wavelength dependence

In our formalism thus far we have avoided mention of wavelength dependence of a body’s surface map. In our derivations we treated the specific intensity at a point on the body’s map as a scalar: a single number corresponding to the total power emitted to space by an infinitesimal area element on the body’s surface. When applying `starry` to actual data, this intensity can either be the power integrated over a range of wavelengths, in which case the light curve has units of flux proper, corresponding to (say) the quantity measured by an instrument performing filter photometry; or the power at a *specific* wavelength, in which case the light curve computed by `starry` has units of *spectral* flux, corresponding to (say) the flux measured in a tiny wavelength bin by a spectrometer. Note, importantly, that in the former case the “surface map” is in reality the integral of the body’s wavelength-dependent specific intensity convolved with the instrument’s spectral response function over a given wavelength range. While `starry` can be used to compute wavelength-dependent light curves by specifying a different map for each wavelength, this is at present inefficient, since `starry` re-computes the occultation integrals for each wavelength bin. The next version of `starry` will include functionality to allow users to easily and quickly compute spectra of celestial bodies in occultation.

### 5.2. Reflectance light curves

At present, `starry` can only compute thermal phase curves and occultation light curves for planets and moons. Reflectance light curves are significantly more difficult to compute analytically because of the sharp discontinuity in the illumination gradient at the terminator. In principle, the stellar illumination pattern could be modeled with a high order spherical harmonic expansion, but this approach cannot accurately capture the sharp day/night transition at the terminator and typically leads to spurious ringing on the night side. A better approach is to treat the terminator as one of the boundaries of the surface integral and use Green’s theorem to compute the line integral about this elliptical curve. This will be the topic of a future paper and will be implemented in future versions of the code.

### 5.3. Non-negative surface maps

While spherical harmonics are a convenient way to approximate surface maps of celestial bodies, it is not trivial to ensure that a given spherical harmonic expansion  $\mathbf{y}$  evaluates to non-negative values everywhere on the unit sphere. This is because there is no analytical way to compute the extrema of a function of spherical harmonics of arbitrary order. This fact makes it difficult to enforce the physical prior that the specific intensity of a celestial body cannot be negative, which could be desirable when fitting a model to real data. The minimum can, of course, be found numerically, although this is slow and should probably not be done repeatedly during optimization

to enforce a prior. Nevertheless, users can request to offset the  $Y_{0,0}$  coefficient of a given map to make it non-negative over the entire domain by typing

```
40 m.nonnegative()
```

This method evaluates the surface map on a coarse grid, locates the approximate location of the minimum, and performs a gradient-descent optimization to locate the global minimum of the map. The  $Y_{0,0}$  coefficient is then offset to enforce non-negative intensities everywhere.

#### 5.4. Very large occultors

When the occultor becomes much larger than the occulted body ( $r_o \gg 1$ ), the analytical solutions to the occultation integrals may become numerically unstable when the map degree  $l$  is large. This is due to the propagation of round-off error in the recurrence relations, which we mitigate with careful Taylor expansions and reparameterizations of the equations. We discuss this at length in Appendix D.2.3 and summarize the results in Figure 12. In general, numerical stability is not likely to be an issue for  $l \leq 8$  and  $r_o \lesssim 500$ , for which the maximum fractional error due to round-off is on the order of one part per thousand, which in the case of exoplanets is likely far below the detectability limits of telescopes in the foreseeable future. Nevertheless, users can bypass these numerical issues by requesting that calculations be performed using multiple precision:

```
41 m.use_mp = True
```

which defaults to quadruple (128-bit) floating point precision. We caution, however, that this will increase computation time by at least an order of magnitude.

#### 5.5. Three-body events

The occultation formalism developed in this paper applies specifically to the case of a single occultor, so `starry` cannot at present handle mutual occultations involving more than two bodies. However, even for an arbitrary number of bodies the problem is still analytical, since Green’s theorem may be employed in the same way, but instead evaluating the line integrals along the more complex network of arcs defining the edges of the visible portion of the body’s surface. This was first noted by Pál (2012), whose `mttr` code computes analytical transit light curves for mutually overlapping bodies such as a transiting planet with a moon. Future versions of `starry` will extend the calculations to this general case.

## 6. CONCLUSIONS

In this paper, we derived a formalism to compute analytical thermal light curves of celestial bodies in occultation, provided their specific intensity maps can be expressed as a sum of spherical harmonics. Our expressions extend the analytical results of

the [Mandel & Agol \(2002\)](#) transit model for limb-darkened stars to transits and occultations of celestial bodies whose surface maps are not radially symmetric and/or possess higher order features, and are thus generally applicable to stars, planets, and moons. We derived recurrence relations to quickly compute occultation light curves for surface maps expressed at arbitrary spherical harmonic degree. We showed, in particular, that the flux contribution from higher degree terms depends on the same elliptic integrals as the linear limb darkening term, so these need only be evaluated once per light curve cadence. This results in evaluation times for higher degree maps that are extremely fast, and only marginally slower than in the quadratic limb-darkening case. In the limit of zero occultor size, our expressions trivially reduce to equations for thermal phase curves of celestial bodies.

We introduced `starry`, a Python-wrapped photodynamical model coded in C++ that can be used to compute phase curves and occultation light curves for individual celestial bodies or entire exoplanet systems. `starry` computes transits, secondary eclipses, phase curves, and planet-planet occultations analytically and is comparable in speed to other transit-modeling packages such as `batman` ([Kreidberg 2015](#)). Because the light curves are all analytical, `starry` can also easily compute analytical gradients of the light curves with respect to all input parameters via autodifferentiation, facilitating its interface with gradient-based inference schemes such as Hamiltonian Monte Carol (HMC) or gradient-descent optimization methods.

Although we have in mind the application of this `starry` to exoplanets, it could in principle be applied to eclipsing binaries as well. If the deformation of the body is small and reflection is negligible, as is the case for long orbital periods, then the surface brightness of each star can be decomposed into spherical harmonics, and the `starry` formalism may be used to integrate their phase curves and eclipses. One could imagine applying `starry`, for instance, to secondary eclipses of white dwarfs to search for non-uniform surface brightness.

At present, `starry` supports only monochromatic surface maps, making it ideally suited for the modeling of light curves collected via filter photometry, but future work will extend it to spectrophotometry. `starry` is also limited to thermal light curves of planets and moons, since the discontinuity in the gradient of the illumination pattern at the terminator makes it more challenging to analytically solve the surface integrals in reflected light. However, an analytical solution is likely to exist, and future work aims to extend `starry` to this case.

The upcoming James Webb Space Telescope (JWST) and eventual next-generation telescopes such as the Origins Space Telescope (OST) will measure exoplanet secondary eclipses and phase curves in the thermal infrared to unprecedented precision. `starry` can compute extremely fast and high-precision models for these light curves, enabling the reconstruction of two-dimensional maps of these alien worlds.

Some of the results in this paper have been derived using the HEALPix (Górski et al. 2005) package.

## REFERENCES

- Abramowitz, M., & Stegun, I. A. 1970, Handbook of Mathematical Functions: With Formulas, Graphs, and Mathematical Tables (Washington, D.C.: U.S. Dept. of Commerce, National Bureau of Standards)
- Collado, J. R. A., et al. 1989, Computer Physics Communications, 52, 323
- Cowan, N. B., et al. 2013, MNRAS, 434, 2465
- Cowan, N. B., & Fujii, Y. 2017, Mapping Exoplanets, 147
- Cowan, N. B., et al. 2012, ApJ, 757, 80
- de Wit, J., et al. 2012, A&A, 548, A128
- Fujii, Y., et al. 2017, AJ, 154, 189
- Górski, K. M., et al. 2005, ApJ, 622, 759
- Gradshteyn, I., & Ryzhik, I. 1994, Table of Integrals, Series, and Products, 5th edn., ed. A. Jeffrey (Academic Press)
- Jakob, W., et al. 2017, pybind11: Seamless operability between C++11 and Python, v2.2, GitHub. <https://github.com/pybind/pybind11>
- Jones, E., et al. 2001, SciPy: Open source scientific tools for Python, v1.0.0, Online. <http://www.scipy.org/>
- Knutson, H. A., et al. 2007, Nature, 447, 183
- Kreidberg, L. 2015, PASP, 127, 1161
- Luger, R., & Agol, E. 2018, ApJ, XX, YY
- Luger, R., et al. 2017, ApJ, 851, 94
- Majeau, C., et al. 2012, ApJL, 747, L20
- Mandel, K., & Agol, E. 2002, ApJL, 580, L171
- Pál, A. 2012, MNRAS, 420, 1630
- Schäling, B. 2014, The Boost C++ Libraries (XML Press)
- Steinborn, E., & Ruedenberg, K. 1973, 7, 1
- Varshalovich, D. A., et al. 1988, Quantum Theory of Angular Momentum: Irreducible Tensors, Spherical Harmonics, Vector Coupling Coefficients, 3nj Symbols (Singapore: World Scientific)
- Wolfram Research, Inc. 2016, Mathematica, v11.0, Champaign, IL

## APPENDIX

### A. SPHERICAL HARMONICS

In spherical coordinates, the spherical harmonics may be compactly represented as in Equation (1). The formalism in this paper requires us to express them in Cartesian form, which is somewhat more cumbersome but still tractable. Using Equation (2) and expanding Equation (1) via the multiple angle formula, we obtain

$$Y_{lm}(x, y, z) = \left( \frac{1}{\sqrt{1-z^2}} \right)^{|m|} \begin{cases} \bar{P}_{lm}(z) \sum_{j \text{ even}}^m (-1)^{\frac{j}{2}} \binom{m}{j} x^{m-j} y^j & m \geq 0 \\ \bar{P}_{l|m|}(z) \sum_{j \text{ odd}}^{|m|} (-1)^{\frac{j-1}{2}} \binom{|m|}{j} x^{|m|-j} y^j & m < 0, \end{cases} \quad (\text{A1})$$

where  $\binom{m}{j}$  is the binomial coefficient. The normalized associated Legendre functions are defined as

$$\bar{P}_{lm}(z) = A_{lm} \left( \sqrt{1-z^2} \right)^m \frac{d^m}{dz^m} \left[ \frac{1}{2^l l!} \frac{d^l}{dz^l} (z^2 - 1)^l \right], \quad (\text{A2})$$

where

$$A_{lm} = \sqrt{\frac{(2 - \delta_{m0})(2l+1)(l-m)!}{4\pi(l+m)!}}. \quad (\text{A3})$$

Expanding out the  $z$  derivatives, we obtain

$$\bar{P}_{lm}(z) = A_{lm} \left( \sqrt{1-z^2} \right)^m \sum_{k=0}^{l-m} \frac{2^l \left( \frac{l+m+k-1}{2} \right)!}{k!(l-m-k)! \left( \frac{-l+m+k-1}{2} \right)!} z^k, \quad (\text{A4})$$

which we combine with the previous results to write

$$Y_{lm}(x, y, z) = \begin{cases} \sum_{j \text{ even}}^m \sum_{k=0}^{l-m} (-1)^{\frac{j}{2}} A_{lm} B_{lm}^{jk} x^{m-j} y^j z^k & m \geq 0 \\ \sum_{j \text{ odd}}^{|m|} \sum_{k=0}^{l-|m|} (-1)^{\frac{j-1}{2}} A_{l|m|} B_{l|m|}^{jk} x^{|m|-j} y^j z^k & m < 0 \end{cases} \quad (\text{A5})$$


where

$$B_{lm}^{jk} = \frac{2^l m! \binom{l+m+k-1}{2}!}{j! k! (m-j)! (l-m-k)! \binom{-l+m+k-1}{2}!}. \quad (\text{A6})$$

Since we are confined to the surface of the unit sphere, we have  $z = \sqrt{1 - x^2 - y^2}$  and we may expand  $z^k$  using the binomial theorem:

$$\begin{aligned} z^k &= (1 - x^2 - y^2)^{\frac{k}{2}} \\ &= \begin{cases} \sum_{p \text{ even}}^k \sum_{q \text{ even}}^p (-1)^{\frac{p}{2}} C_{pq}^k x^{p-q} y^q & k \text{ even} \\ \sum_{p \text{ even}}^{k-1} \sum_{q \text{ even}}^p (-1)^{\frac{p}{2}} C_{pq}^{k-1} x^{p-q} y^q \sqrt{1 - x^2 - y^2} & k \text{ odd}, \end{cases} \end{aligned} \quad (\text{A7})$$

where

$$C_{pq}^k = \frac{\binom{k}{2}!}{\binom{q}{2}! \binom{k-p}{2}! \binom{p-q}{2}!}. \quad (\text{A8})$$

This gives us an expression for the spherical harmonics  $Y_{lm}$  as a function of  $x$  and  $y$  only:

$$Y_{lm}(x, y) = \begin{cases} \sum_{j \text{ even}}^m \sum_{k \text{ even}}^{l-m} \sum_{p \text{ even}}^k \sum_{q \text{ even}}^p (-1)^{\frac{j+p}{2}} A_{lm} B_{lm}^{jk} C_{pq}^k x^{m-j+p-q} y^{j+q} + \\ \sum_{j \text{ even}}^m \sum_{k \text{ odd}}^{l-m} \sum_{p \text{ even}}^{k-1} \sum_{q \text{ even}}^p (-1)^{\frac{j+p}{2}} A_{lm} B_{lm}^{jk} C_{pq}^{k-1} x^{m-j+p-q} y^{j+q} z & m \geq 0 \\ \sum_{j \text{ odd}}^{|m|} \sum_{k \text{ even}}^{l-|m|} \sum_{p \text{ even}}^k \sum_{q \text{ even}}^p (-1)^{\frac{j+p-1}{2}} A_{l|m|} B_{l|m|}^{jk} C_{pq}^k x^{|m|-j+p-q} y^{j+q} + \\ \sum_{j \text{ odd}}^{|m|} \sum_{k \text{ odd}}^{l-|m|} \sum_{p \text{ even}}^{k-1} \sum_{q \text{ even}}^p (-1)^{\frac{j+p-1}{2}} A_{l|m|} B_{l|m|}^{jk} C_{pq}^{k-1} x^{|m|-j+p-q} y^{j+q} z & m < 0 \end{cases} \quad (\text{A9})$$


where  $z = z(x, y) = \sqrt{1 - x^2 - y^2}$ . Evaluating the nested sums may be computationally slow, but these operations need only be performed a single time to construct our change of basis matrix (Appendix 2.3).

## B. CHANGE OF BASIS

In this section we discuss how to compute the change of basis matrices  $\mathbf{A}_1$  and  $\mathbf{A}_2$  from §2.3 and provide links to **Mathematica** scripts to compute them. Recall that the columns of the change of basis matrix from spherical harmonics to polynomials,  $\mathbf{A}_1$ , are just the polynomial vectors corresponding to each of the spherical harmonics in Equation (4). From Equations (7) and (A9), we can calculate the first few spherical harmonics and their corresponding polynomial vectors:

$$\begin{aligned} Y_{0,0} &= \frac{1}{2\sqrt{\pi}} & \mathbf{p} &= \frac{1}{2\sqrt{\pi}} \begin{pmatrix} 1 & 0 & 0 & 0 & \dots \end{pmatrix}^T \\ Y_{1,-1} &= \frac{\sqrt{3}}{2\sqrt{\pi}} y & \mathbf{p} &= \frac{1}{2\sqrt{\pi}} \begin{pmatrix} 0 & 0 & 0 & \sqrt{3} & \dots \end{pmatrix}^T \\ Y_{1,0} &= \frac{\sqrt{3}}{2\sqrt{\pi}} z & \mathbf{p} &= \frac{1}{2\sqrt{\pi}} \begin{pmatrix} 0 & 0 & \sqrt{3} & 0 & \dots \end{pmatrix}^T \\ Y_{1,1} &= \frac{\sqrt{3}}{2\sqrt{\pi}} x & \mathbf{p} &= \frac{1}{2\sqrt{\pi}} \begin{pmatrix} 0 & \sqrt{3} & 0 & 0 & \dots \end{pmatrix}^T \\ Y_{2,-2} &= \dots & \mathbf{p} &= \dots \end{aligned} \tag{B10}$$

From these we can construct  $\mathbf{A}_1$ . As an example, for spherical harmonics up to degree  $l_{\max} = 2$ , this is

$$\mathbf{A}_1 = \frac{1}{2\sqrt{\pi}} \begin{pmatrix} 1 & 0 & 0 & 0 & 0 & 0 & \sqrt{5} & 0 & 0 \\ 0 & 0 & 0 & \sqrt{3} & 0 & 0 & 0 & 0 & 0 \\ 0 & 0 & \sqrt{3} & 0 & 0 & 0 & 0 & 0 & 0 \\ 0 & \sqrt{3} & 0 & 0 & 0 & 0 & 0 & 0 & 0 \\ 0 & 0 & 0 & 0 & 0 & 0 & -\frac{3\sqrt{5}}{2} & 0 & \frac{\sqrt{15}}{2} \\ 0 & 0 & 0 & 0 & 0 & 0 & 0 & \sqrt{15} & 0 \\ 0 & 0 & 0 & 0 & \sqrt{15} & 0 & 0 & 0 & 0 \\ 0 & 0 & 0 & 0 & 0 & \sqrt{15} & 0 & 0 & 0 \\ 0 & 0 & 0 & 0 & 0 & 0 & -\frac{3\sqrt{5}}{2} & 0 & -\frac{\sqrt{15}}{2} \end{pmatrix}. \tag{B11}$$


We compute the change of basis matrix from polynomials to Green's polynomials,  $\mathbf{A}_2$ , in a similar manner. In practice, it is easier to express the elements of the Green's basis  $\tilde{\mathbf{g}}$  in terms of the elements of the polynomial basis  $\tilde{\mathbf{p}}$  and use those to populate the columns of the matrix  $\mathbf{A}_2^{-1}$ . Continuing our example for  $l_{\max} = 2$ , our second

change of basis matrix is

$$\mathbf{A}_2 = \begin{pmatrix} 1 & 0 & 0 & 0 & 0 & 0 & 0 & 0 & 0 \\ 0 & \frac{1}{2} & 0 & 0 & 0 & 0 & 0 & 0 & 0 \\ 0 & 0 & 1 & 0 & 0 & 0 & 0 & 0 & 0 \\ 0 & 0 & 0 & 1 & 0 & 0 & 0 & 0 & 0 \\ 0 & 0 & 0 & 0 & \frac{1}{3} & 0 & 0 & 0 & 0 \\ 0 & 0 & 0 & 0 & 0 & -\frac{1}{3} & 0 & 0 & 0 \\ 0 & 0 & 0 & 0 & 0 & 0 & \frac{1}{2} & 0 & 0 \\ 0 & 0 & 0 & 0 & 0 & 0 & 0 & \frac{1}{3} & 0 \\ 0 & 0 & 0 & 0 & 0 & 0 & 0 & 0 & 1 \end{pmatrix}. \quad (\text{B12})$$


Finally, recall that the complete change of basis matrix from spherical harmonics to Green's polynomials,  $\mathbf{A}$ , is just the matrix product of  $\mathbf{A}_1$  and  $\mathbf{A}_2$ . For  $l_{\max} = 2$ , we have

$$\mathbf{A} = \frac{1}{2\sqrt{\pi}} \begin{pmatrix} 1 & 0 & 0 & 0 & 0 & 0 & \frac{\sqrt{5}}{2} & 0 & 0 \\ 0 & 0 & 0 & \sqrt{3} & 0 & 0 & 0 & 0 & 0 \\ 0 & 0 & \sqrt{3} & 0 & 0 & 0 & 0 & 0 & 0 \\ 0 & \frac{\sqrt{3}}{2} & 0 & 0 & 0 & 0 & 0 & 0 & 0 \\ 0 & 0 & 0 & 0 & 0 & 0 & -\frac{3\sqrt{5}}{4} & 0 & \frac{\sqrt{15}}{2} \\ 0 & 0 & 0 & 0 & 0 & 0 & 0 & \sqrt{\frac{5}{3}} & 0 \\ 0 & 0 & 0 & 0 & \sqrt{\frac{5}{3}} & 0 & 0 & 0 & 0 \\ 0 & 0 & 0 & 0 & 0 & -\sqrt{\frac{5}{3}} & 0 & 0 & 0 \\ 0 & 0 & 0 & 0 & 0 & 0 & -\frac{3\sqrt{5}}{4} & 0 & -\frac{\sqrt{15}}{2} \end{pmatrix}. \quad (\text{B13})$$


## C. ROTATION OF SPHERICAL HARMONICS

### C.1. Euler angles

Collado et al. (1989) derived expressions for the rotation matrices for the real spherical harmonics of a given degree  $l$  from the corresponding complex rotation matrices (Steinborn & Ruedenberg 1973):

$$\mathbf{R}^l = \mathbf{U}^{-1} \mathbf{D}^l \mathbf{U} \quad (\text{C14})$$

where

$$\begin{aligned} \mathbf{D}_{m,m'}^l &= e^{-i(\alpha m' + \gamma m)} (-1)^{m'+m} \sqrt{(l-m)!(l+m)!(l-m')!(l+m')!} \\ &\times \sum_k (-1)^k \frac{\cos\left(\frac{\beta}{2}\right)^{2l+m-m'-2k} \sin\left(\frac{\beta}{2}\right)^{-m+m'+2k}}{k!(l+m-k)!(l-m'-k)!(m'-m+k)!} \end{aligned} \quad (\text{C15})$$

is the rotation matrix for the complex spherical harmonics of degree  $l$  and

$$\mathbf{U} = \frac{1}{\sqrt{2}} \begin{pmatrix} \ddots & & & & & & \ddots \\ & i & & & & & 1 \\ & & i & & & & 1 \\ & & & i & & 1 & \\ & & & & \sqrt{2} & & \\ & & & i & & -1 & \\ & & -i & & & & 1 \\ & i & & & & & -1 \\ \ddots & & & & & & \ddots \end{pmatrix}. \quad (\text{C16})$$

describes the transformation from complex to real spherical harmonics. In Equation (C15) above,  $\alpha$ ,  $\beta$ , and  $\gamma$  are the (proper) Euler angles for rotation in the  $z-y-z$  convention. To obtain a rotation matrix for an arbitrary vector  $\mathbf{y}$  with spherical harmonics of different orders up to  $l = l_{\max}$ , we define the block-diagonal matrix  $\mathbf{R}$ :

$$\mathbf{R} = \begin{pmatrix} \mathbf{R}^0 & & & \\ & \mathbf{R}^1 & & \\ & & \mathbf{R}^2 & \\ & & & \mathbf{R}^3 \\ & & & & \ddots \end{pmatrix}. \quad (\text{C17})$$


Rotation of  $\mathbf{y}$  by the Euler angles  $\alpha$ ,  $\beta$ , and  $\gamma$  is performed via Equation (16) with  $\mathbf{R}$  given by Equation (C17).

## C.2. Axis-angle

It is often more convenient to define a rotation by an axis  $\mathbf{u}$  and an angle  $\theta$  of rotation about that axis. Given a unit vector  $\mathbf{u}$  and an angle  $\theta$ , we can find the corresponding Euler angles by comparing the 3-dimensional Cartesian rotation

matrices for both systems,

$$\mathbf{P} = \begin{pmatrix} c_\theta + u_x^2(1 - c_\theta) & u_x u_y (1 - c_\theta) - u_z s_\theta & u_x u_z (1 - c_\theta) + u_y s_\theta \\ u_y u_x (1 - c_\theta) + u_z s_\theta & c_\theta + u_y^2 (1 - c_\theta) & u_y u_z (1 - c_\theta) - u_x s_\theta \\ u_z u_x (1 - c_\theta) - u_y s_\theta & u_z u_y (1 - c_\theta) + u_x s_\theta & c_\theta + u_z^2 (1 - c_\theta) \end{pmatrix} \quad (\text{C18})$$

for axis-angle rotations and

$$\mathbf{Q} = \begin{pmatrix} c_\alpha c_\beta c_\gamma - s_\alpha s_\gamma & -c_\gamma s_\alpha - c_\alpha c_\beta s_\gamma & c_\alpha s_\beta \\ c_\alpha s_\gamma + c_\beta c_\gamma s_\alpha & c_\alpha c_\gamma - c_\beta s_\alpha s_\gamma & s_\alpha s_\beta \\ -c_\gamma s_\beta & s_\beta s_\gamma & c_\beta \end{pmatrix}, \quad (\text{C19})$$

for Euler rotations, where  $c. \equiv \cos(\cdot)$  and  $s. \equiv \sin(\cdot)$ . Comparison of the two matrices gives us expressions for the Euler angles in terms of  $\mathbf{u}$  and  $\theta$ :

$$\begin{aligned} \cos \alpha &= \frac{P_{0,2}}{\sqrt{P_{0,2}^2 + P_{1,2}^2}} & \cos \beta &= P_{2,2} & \cos \gamma &= -\frac{P_{2,0}}{\sqrt{P_{2,0}^2 + P_{2,1}^2}}. \\ \sin \alpha &= \frac{P_{1,2}}{\sqrt{P_{0,2}^2 + P_{1,2}^2}} & \sin \beta &= \sqrt{1 - P_{2,2}^2} & \sin \gamma &= \frac{P_{2,1}}{\sqrt{P_{2,0}^2 + P_{2,1}^2}}. \end{aligned} \quad (\text{C20})$$


Thus, given a spherical harmonic vector  $\mathbf{y}$ , we can calculate how it transforms under rotation by an angle  $\theta$  about an axis  $\mathbf{u}$  by first computing the Euler angles (Equation C20) and using those to construct the spherical harmonic rotation matrix (Equation C17).

#### D. COMPUTING THE SOLUTION VECTOR $s_n$

Here we seek a solution to Equation (30), which gives the total flux during an occultation of the  $n^{\text{th}}$  term in the Green's basis (Equation 11). The primitive integrals  $\mathcal{P}$  and  $\mathcal{G}$  in that equation are given by Equations (31) and (32), with  $\mathbf{G}_n$  defined in Equation (34). Note that all of the terms in Equation (34), with the exception of the  $l = 1, m = 0$  case, are simple polynomials in  $x, y$ , and  $z$ , which facilitates their integration. The  $l = 1, m = 0$  term (corresponding to the  $n = 2$  term in the Green's basis) is more difficult to integrate, but an analytical solution exists (Pál 2012). It is, however, more convenient to note that this term corresponds to a surface map given by the polynomial  $I(x, y) = \tilde{g}_2(x, y) = \sqrt{1 - x^2 - y^2}$ , which is the same function used to model linear limb darkening in stars (Mandel & Agol 2002). We therefore evaluate this term separately in Appendix D.1 below, followed by the general term in Appendix D.2.

### D.1. Linear limb darkening ( $n = 2$ )

From Mandel & Agol (2002), the total flux visible during the occultation of a body whose surface map is given by  $I(x, y) = \sqrt{1 - x^2 - y^2}$  may be computed as

$$s_2 = \frac{2\pi}{3} \left( 1 - \frac{3\Lambda}{2} - \Theta(r - b) \right) \quad (\text{D21})$$

where  $\Theta(\cdot)$  is the Heaviside step function and

$$\Lambda = \begin{cases} \frac{1}{9\pi\sqrt{br}} \left[ \frac{(r+b)^2 - 1}{r+b} \left( -2r(2(r+b)^2 + (r+b)(r-b) - 3)K(k^2) \right. \right. \\ \left. \left. + 3(b-r)\Pi(k^2(b+r)^2, k^2) \right) - 4br(4 - 7r^2 - b^2)E(k^2) \right] & k^2 < 1 \\ \frac{2}{9\pi} \left[ (1 - (r+b)^2) \left( \sqrt{1 - (b-r)^2} K\left(\frac{1}{k^2}\right) + 3 \left( \frac{b-r}{(b+r)\sqrt{1 - (b-r)^2}} \right) \right. \right. \\ \left. \left. \times \Pi\left(\frac{1}{k^2(b+r)^2}, \frac{1}{k^2}\right) \right) - \sqrt{1 - (b-r)^2}(4 - 7r^2 - b^2)E\left(\frac{1}{k^2}\right) \right] & k^2 \geq 1 \end{cases} \quad (\text{D22})$$

with

$$k^2 = \frac{1 - r^2 - b^2 + 2br}{4br}. \quad (\text{D23})$$

In the expressions above,  $K(\cdot)$ ,  $E(\cdot)$ , and  $\Pi(\cdot, \cdot)$  are the complete elliptic integrals of the first, second kind, and third kind, respectively, defined as

$$\begin{aligned} K(k^2) &\equiv \int_0^{\frac{\pi}{2}} \frac{d\varphi}{\sqrt{1 - k^2 \sin^2 \varphi}} \\ E(k^2) &\equiv \int_0^{\frac{\pi}{2}} \sqrt{1 - k^2 \sin^2 \varphi} d\varphi \\ \Pi(n, k^2) &\equiv \int_0^{\frac{\pi}{2}} \frac{d\varphi}{(1 - n \sin^2 \varphi) \sqrt{1 - k^2 \sin^2 \varphi}}. \end{aligned} \quad (\text{D24})$$

D.2. All other terms  
 D.2.1. Setting up the equations

We evaluate all other terms in  $s_n$  by integrating the primitive integrals of  $\mathbf{G}_n$ . These are given by

$$\mathcal{P}(\mathbf{G}_n) = \begin{cases} + \int_{\pi-\phi}^{2\pi+\phi} (rc_\varphi)^{\frac{\mu+2}{2}} (b + rs_\varphi)^{\frac{\nu}{2}} rc_\varphi d\varphi & \nu \text{ even} \\ - \int_{\pi-\phi}^{2\pi+\phi} (rc_\varphi)^{l-2} (1-r^2-b^2-2brs_\varphi)^{\frac{3}{2}} rs_\varphi d\varphi & \nu \text{ odd, } \mu = 1, l \text{ even} \\ - \int_{\pi-\phi}^{2\pi+\phi} (rc_\varphi)^{l-3} (b + rs_\varphi) (1-r^2-b^2-2brs_\varphi)^{\frac{3}{2}} rs_\varphi d\varphi & \nu \text{ odd, } \mu = 1, l \text{ odd} \\ + \int_{\pi-\phi}^{2\pi+\phi} (rc_\varphi)^{\frac{\mu-3}{2}} (b + rs_\varphi)^{\frac{\nu-1}{2}} (1-r^2-b^2-2brs_\varphi)^{\frac{3}{2}} rc_\varphi d\varphi & \text{otherwise} \end{cases} \quad (\text{D25})$$

and

$$\mathcal{Q}(\mathbf{G}_n) = \begin{cases} + \int_{\pi-\lambda}^{2\pi+\lambda} c_\varphi^{\frac{\mu+2}{2}} s_\varphi^{\frac{\nu}{2}} c_\varphi d\varphi & \nu \text{ even} \\ 0 & \text{otherwise,} \end{cases} \quad (\text{D26})$$

where we have used the fact that the line integral of any function proportional to  $z$  taken along the limb of the occulted planet (where  $z = \sqrt{1-x^2-y^2} = 0$ ) is zero. For convenience, let us introduce the integrals

$$\mathcal{H}_{u,v} = \int_{\pi-\lambda}^{2\pi+\lambda} c_\varphi^u s_\varphi^v d\varphi \quad (\text{D27})$$

$$\mathcal{I}_{u,v} = \int_{\pi-\phi}^{2\pi+\phi} c_\varphi^u s_\varphi^v d\varphi \quad (\text{D28})$$

$$\mathcal{J}_{u,v} = \int_{\pi-\phi}^{2\pi+\phi} c_\varphi^u s_\varphi^v (1 - r^2 - b^2 - 2brs_\varphi)^{\frac{3}{2}} d\varphi, \quad (\text{D29})$$

along with the expressions

$$\mathcal{K}_{u,v} = \sum_{i=0}^v \binom{v}{i} \left(\frac{b}{r}\right)^{v-i} \mathcal{I}_{u,i}. \quad (\text{D30})$$

$$\mathcal{L}_{u,v} = \sum_{i=0}^v \binom{v}{i} \left(\frac{b}{r}\right)^{v-i} \mathcal{J}_{u,i}. \quad (\text{D31})$$

With some algebra, we may therefore write

$$\mathcal{P}(\mathbf{G}_n) = \begin{cases} r^{l+2} \mathcal{K}_{\frac{\mu+4}{2}, \frac{\nu}{2}} & \nu \text{ even} \\ -r^{l-1} \mathcal{J}_{l-2,1} & \nu \text{ odd, } \mu = 1, l \text{ even} \\ -r^{l-2} (b\mathcal{J}_{l-3,1} + r\mathcal{J}_{l-3,2}) & \nu \text{ odd, } \mu = 1, l \text{ odd} \\ r^{l-1} \mathcal{L}_{\frac{\mu-1}{2}, \frac{\nu-1}{2}} & \text{otherwise} \end{cases} \quad (\text{D32})$$


and

$$\mathcal{Q}(\mathbf{G}_n) = \begin{cases} \mathcal{H}_{\frac{\mu+4}{2}, \frac{\nu}{2}} & \nu \text{ even} \\ 0 & \nu \text{ odd.} \end{cases} \quad (\text{D33})$$

The solution to the occultation problem is therefore a matter of finding expressions for the integrals  $\mathcal{H}_{u,v}$ ,  $\mathcal{I}_{u,v}$ , and  $\mathcal{J}_{u,v}$ .

### D.2.2. Solving the integrals

Fortunately,  $\mathcal{H}_{u,v}$  and  $\mathcal{I}_{u,v}$  evaluate to terms containing only sines and cosines of  $\lambda$  and  $\phi$ , respectively. Pál (2012) derived simple recurrence relations for these terms:

$$\mathcal{H}_{u,v} = \begin{cases} 0 & u \text{ odd} \\ 2\lambda + \pi & u = v = 0 \\ -2 \cos \lambda & u = 0, v = 1 \\ \frac{2}{u+v} (\cos \lambda)^{u-1} (\sin \lambda)^{v+1} + \frac{u-1}{u+v} \mathcal{H}_{u-2,v} & u \geq 2 \\ -\frac{2}{u+v} (\cos \lambda)^{u+1} (\sin \lambda)^{v-1} + \frac{v-1}{u+v} \mathcal{H}_{u,v-2} & v \geq 2 \end{cases} \quad (\text{D34})$$


and

$$\mathcal{I}_{u,v} = \begin{cases} 0 & u \text{ odd} \\ 2\phi + \pi & u = v = 0 \\ -2 \cos \phi & u = 0, v = 1 \\ \frac{2}{u+v} (\cos \phi)^{u-1} (\sin \phi)^{v+1} + \frac{u-1}{u+v} \mathcal{I}_{u-2,v} & u \geq 2 \\ -\frac{2}{u+v} (\cos \phi)^{u+1} (\sin \phi)^{v-1} + \frac{v-1}{u+v} \mathcal{I}_{u,v-2} & v \geq 2. \end{cases} \quad (\text{D35})$$


Conversely, because of the term raised to the  $3/2$  power in Equation (D29),  $\mathcal{J}_{u,v}$  is significantly more difficult to compute. With some tedious algebraic manipulation, and using recurrence relations for expressions with integrands of the form  $\cos^p \varphi \sin^q \varphi (1 - \chi^2 \sin^2 \varphi)^{\frac{3}{2}}$  (Gradshteyn & Ryzhik 1994), we may write

$$\mathcal{J}_{u,v} = 2^{u+3} (br)^{\frac{3}{2}} \sum_{i=0}^v \binom{v}{i} (-1)^{i-v-u} \mathcal{M}_{u+2i, u+2v-2i} \quad (\text{D36})$$


where

$$\mathcal{M}_{p,q} = \begin{cases} 0 & p \text{ odd or } q \text{ odd} \\ \frac{d_1 \mathcal{M}_{p,q-2} + d_2 \mathcal{M}_{p,q-4}}{p+q+3} & q \geq 4 \\ \frac{d_3 \mathcal{M}_{p-2,q} + d_4 \mathcal{M}_{p-4,q}}{p+q+3} & p \geq 4 \end{cases} \quad (\text{D37})$$


with

$$\begin{aligned} d_1 &= q + 2 + (p + q - 2)(1 - k^2) \\ d_2 &= (3 - q)(1 - k^2) \\ d_3 &= 2p + q - (p + q - 2)(1 - k^2) \\ d_4 &= (3 - p)k^2 \end{aligned} \quad (\text{D38})$$

and  $k^2$  defined as in Equation (D23). These recurrence relations require four initial conditions:

$$\begin{aligned} \mathcal{M}_{0,0} &= \frac{8 - 12k^2}{3}\mathcal{E}_1 + \frac{-8 + 16k^2}{3}\mathcal{E}_2 \\ \mathcal{M}_{0,2} &= \frac{8 - 24k^2}{15}\mathcal{E}_1 + \frac{-8 + 28k^2 + 12k^4}{15}\mathcal{E}_2 \\ \mathcal{M}_{2,0} &= \frac{32 - 36k^2}{15}\mathcal{E}_1 + \frac{-32 + 52k^2 - 12k^4}{15}\mathcal{E}_2 \\ \mathcal{M}_{2,2} &= \frac{32 - 60k^2 + 12k^4}{105}\mathcal{E}_1 + \frac{-32 + 76k^2 - 36k^4 + 24k^6}{105}\mathcal{E}_2, \end{aligned} \quad (\text{D39})$$


where we defined the elliptic functions

$$\mathcal{E}_1 = \begin{cases} (1 - k^2)K(k^2) & k^2 < 1 \\ 0 & k^2 = 1 \\ \frac{1 - k^2}{\sqrt{k^2}}K\left(\frac{1}{k^2}\right) & k^2 \geq 1 \end{cases} \quad (\text{D40})$$

and

$$\mathcal{E}_2 = \begin{cases} E(k^2) & k^2 < 1 \\ 0 & k^2 = 1 \\ \sqrt{k^2}E\left(\frac{1}{k^2}\right) + \frac{1 - k^2}{\sqrt{k^2}}K\left(\frac{1}{k^2}\right) & k^2 \geq 1. \end{cases} \quad (\text{D41})$$


Interestingly, the elliptic integrals in the expressions above are exactly the same as the ones used to evaluate the  $s_2$  term (Equation D22), so these need only be evaluated *once* when computing the occultation flux of a map of arbitrary degree. Thanks to

the recurrence relations, all other operations required to evaluate  $\mathcal{J}_{u,v}$  are elementary, making the computation of  $s_n$  fast.

### D.2.3. Numerical stability

A few remarks are in order regarding the numerical stability of the solutions presented above. Follow the links to the right of the text for more details on individual cases.

- The solution for  $s_2$  (Equation D21) becomes unstable as  $b \rightarrow r$  because the elliptic integral  $\Pi$  diverges. In the vicinity of  $b = r$  we use Equation (17.7.14) in Abramowitz & Stegun (1970) to express  $\Pi(n, k^2)$  in terms of Heuman's Lambda function.
- The  $s_2$  term is also unstable when  $r$  (and  $b$ ) become much greater than unity, since in this limit  $k^2 \rightarrow 0$  and  $E(k^2) \rightarrow K(k^2) \rightarrow \frac{\pi}{2}$ . Since  $s_2$  depends on (among other things) a function of the difference between these two elliptic integrals, roundoff error in their computation leads to catastrophic cancellation in the result. In order to circumvent this, we re-write Equation (D22) in terms of  $E(k^2) - K(k^2)$  and Taylor expand the expression when  $r > 1$  to high order in  $k^2$ .
- The expression for  $k^2$  (Equation D23) diverges when either  $b = 0$  or  $r = 0$ . Our tests show that the latter case does not introduce significant numerical error when computing the solution vector  $\mathbf{s}$  because of the factors of  $r$  multiplying the integrals in Equation (D32). However, in the limit  $b \rightarrow 0$ , we find that the expressions for  $\mathcal{M}_{p,q}$  (Equation D37) are unstable, leading to large errors in the evaluation of  $\mathcal{J}_{u,v}$  (Equation D36) and thus also in  $\mathcal{P}(\mathbf{G}_n)$  (Equation D32). When  $b = 0$ , the term in parentheses in (Equation D29) vanishes, and we may compute  $\mathcal{J}_{u,v}$  directly as

$$\mathcal{J}_{u,v}(b = 0) = (1 - r^2)^{\frac{3}{2}} \mathcal{I}_{u,v}. \quad (\text{D42})$$

In the vicinity of  $b = 0$ , we instead Taylor expand the integrand in Equation (D29). The top panel in Figure 12 shows the fractional error in the flux (relative to the light curve computed using quadruple precision) as a function of impact parameter for an occultor of radius  $r_o = 0.1$ , after implementing the Taylor expansion described above. Each curve corresponds to a surface map assembled from all coefficients of a given spherical harmonic degree  $l$ . While the instability grows with  $l$ , the fractional error is less than one part per billion (ppb) everywhere for  $l \leq 8$ .

- The recurrence relation (D28) is numerically unstable when  $r > 1$  for large values of  $l$ . The instability results from successive multiplications of  $\sin \phi$  and  $\cos \phi$



proof



(Equation 25), which become extremely close to zero and unity, respectively, as  $r \rightarrow \infty$ . This leads to roundoff error accumulation and causes the expressions to go unstable for large  $l$ . We remedy this by Taylor expanding the limb of the occultor as a quartic and computing the line integral analytically.

- Finally, the recurrence relation (D37) is also numerically unstable for  $r \gg 1$  and large  $l$ . Unfortunately, a quartic expansion of the occultor limb is not feasible, since the resulting line integral is not analytical. Instead, we Taylor expand the elliptic integrals in the expression for  $\mathcal{M}_{p,q}$  to high order in  $k^2$  and tabulate the expansion coefficients in `starry` up to  $l = 8$ . The bottom panel in Figure 12 shows the maximum fractional error in the flux as a function of occultor radius over six orders of magnitude after implementing the quartic expansion for  $\mathcal{I}_{u,v}$  and the Taylor expansion of the elliptic integrals for  $\mathcal{M}_{p,q}$ . Our expressions are stable with sub-ppb precision for all orders through  $l = 8$  for  $r_o < 1$ . For occultors larger than the occulted body, our expressions are accurate to within one part per million (ppm) up to  $l = 5$  and to within one part per thousand (ppt) up to  $l = 8$ . Note, importantly, that the case  $r_o \gg 1$  is typically only relevant to studies of (secondary) eclipses of exoplanets by their host stars, for which ppt precision (measured relative to the *planet* flux) is at present more than sufficient. Moreover, for most physical planet maps the coefficients of the spherical harmonics of high degree are small, such that the error on the total flux will be significantly smaller than that reported above. Figure 13 shows secondary eclipse ingress for the  $l = 8$  Earth being occulted by the Sun ( $r_o \approx 110$ ) alongside the fractional error on the flux. The fractional error is less than 1 ppm everywhere.

The solutions outlined above ensure numerical stability over a wide range of occultor radii and impact parameters, but instabilities may still occur in `starry` when the occultor becomes very large ( $r_o \gg 100$ ) and/or when the map degree is very high ( $l \gtrsim 8$ ). In these cases, users may wish to enable multiple floating-point precision by setting

```
42 m.use_mp = True
```

for a `starry.Map` instance `m`, which by default computes the occultation solution vector `s` using a 128-bit (quadruple) precision type implemented with the `boost` C++ libraries (e.g., Schäling 2014).

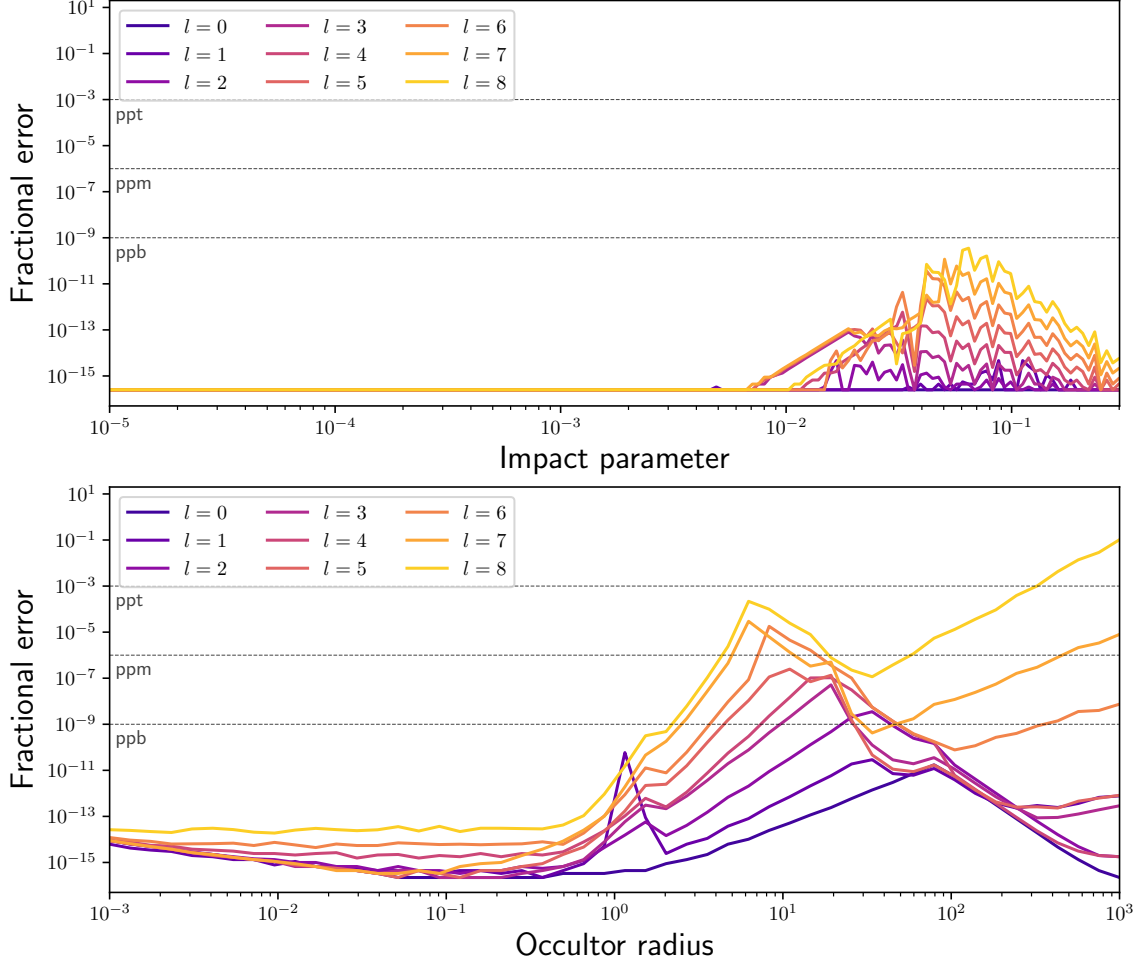


**Figure 12.** Numerical stability tests for `starry`. The error on the flux is computed relative to computations using 128-bit (quadruple) floating point precision. The top panel shows the fractional error as a function of impact parameter for an occultor of radius  $r_o = 0.1$  occulting spherical harmonics of different degrees. The rise in the error toward small impact parameter is due to the instability discussed in the text; as the error approaches the ppb level, `starry` switches to a stable, high order Taylor expansion of the expressions. The bottom panel shows the maximum fractional error on the flux over the entire light curve as a function of the occultor size. The flux is accurate at the sub-ppb level for small ( $r_o \leq 1$ ) occultors and at the sub-ppt level for large ( $r_o \gg 1$ ) occultors up to  $l = 5$ .

&lt;/&gt;

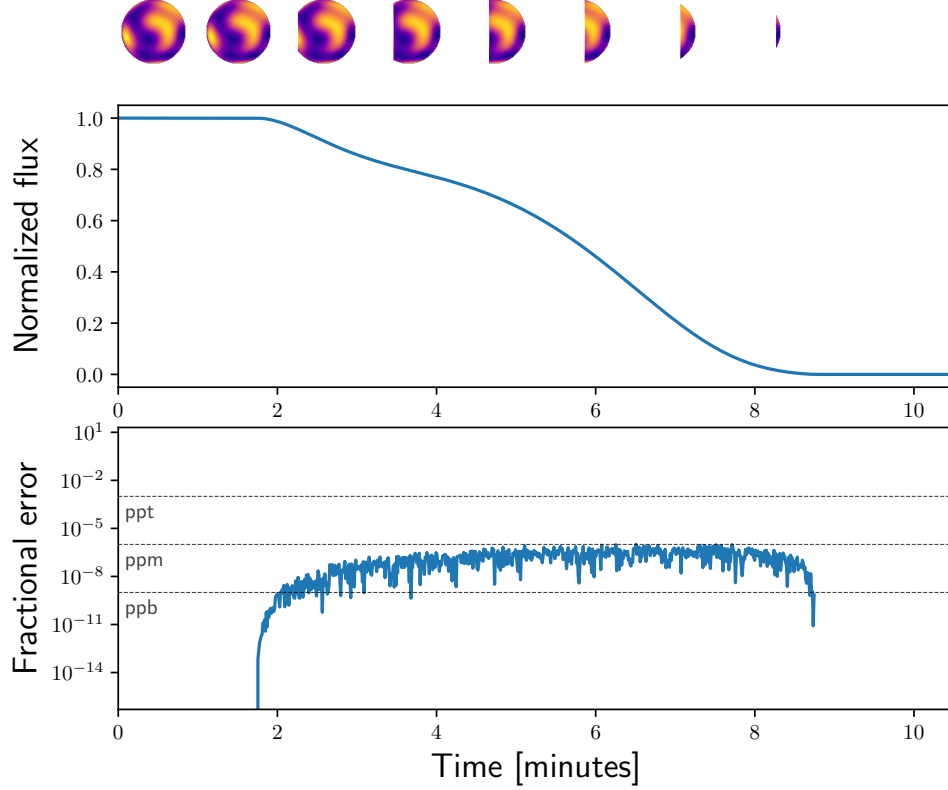


**Figure 13.** Secondary eclipse ingress for the Earth being occulted by the Sun ( $r_o = 110$ ), computed for a  $l = 8$  expansion of the planet's surface map. The fractional error due to floating point precision loss is shown at the bottom and is less than one part per million everywhere.

&lt;/&gt;

**Table 1.** Symbols used in this paper

Symbol	Definition	Reference
$A_{lm}$	Legendre function normalization	Equation (A3)
$\mathbf{A}$	Change of basis matrix: $Y_{lms}$ to Green's polynomials	Equation (14)
$\mathbf{A}_1$	Change of basis matrix: $Y_{lms}$ to polynomials	§2.3
$\mathbf{A}_2$	Change of basis matrix: polynomials to Green's polynomials	§2.3
$b$	Impact parameter in units of occulted body's radius	§3
$B_{lm}^{jk}$	Spherical harmonic normalization	Equation (A6)
$c.$	$\cos(\cdot)$	
$C_{pq}^k$	Expansion coefficient for $z(x, y)$	Equation (A8)
$d$	Dummy coefficient	
$\mathbf{D}^l$	Rotation matrix for the complex spherical harmonics of degree $l$	Equation (C15)
$\mathbf{D} \wedge$	Exterior derivative	Equation (29)
$E(\cdot)$	Complete elliptic integral of the second kind	Equation (D24)
$\mathcal{E}_1$	First elliptic function	Equation (D40)
$\mathcal{E}_2$	Second elliptic function	Equation (D41)
$F$	Total flux seen by observer	Equation (35)
$\tilde{\mathbf{g}}$	Green's basis	Equation (11)
$\mathbf{g}$	Vector in the basis $\tilde{\mathbf{g}}$	
$\mathbf{G}_n$	Anti-exterior derivative of the $n^{\text{th}}$ term in the Green's basis	Equation (34)
$\mathcal{H}_{u,v}$	Occultation integral	Equation (D27)
$I$	Specific intensity, $I(x, y)$	Equation (3)
$\mathcal{I}_{u,v}$	Occultation integral	Equation (D28)
$j$	Dummy index	
$\mathcal{J}_{u,v}$	Occultation integral	Equation (D29)
$k$	Dummy index	
$k^2$	Elliptic parameter	Equation (D23)
$K(\cdot)$	Complete Elliptic integral of the first kind	Equation (D24)
$\mathcal{K}_{u,v}$	Occultation integral	Equation (D30)
$l$	Spherical harmonic degree	Equation (6)
$\mathcal{L}_{u,v}$	Occultation integral	Equation (D31)
$m$	Spherical harmonic order	Equation (6)
$\mathcal{M}_{p,q}$	Occultation integral	Equation (D37)
$n$	Surface map vector index, $n = l^2 + l + m$	Equation (5)
$p$	Dummy index	
$\bar{P}$	Normalized associated Legendre function	Equation (A2)
$\tilde{\mathbf{p}}$	Polynomial basis	Equation (7)
$\mathbf{p}$	Vector in the basis $\tilde{\mathbf{p}}$	
$\mathbf{P}$	Cartesian axis-angle rotation matrix	Equation (C18)
$\mathcal{P}$	Primitive integral along perimiter of occultor	Equation (31)
$q$	Dummy index	

**Table 1** – continued from previous page

Symbol	Definition	Reference
$\mathbf{Q}$	Cartesian Euler angle rotation matrix	Equation (C19)
$\mathcal{Q}$	Primitive integral along perimiter of occulted body	Equation (32)
$r$	Occultor radius in units of occulted body's radius	§3
$\mathbf{r}$	Phase curve solution vector	Equation (19)
$\mathbf{R}$	Rotation matrix for the real spherical harmonics	Equation (C17)
$\mathbf{R}^l$	Rotation matrix for the real spherical harmonics of degree $l$	Equation (C14)
$s.$	$\sin(\cdot)$	
$\mathbf{s}$	Occultation light curve solution vector	Equation (19)
$u_1, u_2$	Quadratic limb darkening coefficients	Equation (37)
$\mathbf{u}$	Unit vector corresponding to the axis of rotation	§C.2
$\mathbf{U}$	Complex to real spherical harmonics transform matrix	Equation (C16)
$x$	Cartesian coordinate	Equation (2)
$y$	Cartesian coordinate	Equation (2)
$Y_{l,m}$	Spherical harmonic of degree $l$ and order $m$	Equation (A1)
$\tilde{\mathbf{y}}$	Spherical harmonic basis	Equation (4)
$\mathbf{y}$	Vector in the basis $\tilde{\mathbf{y}}$	
$z$	Cartesian coordinate, $z = \sqrt{1 - x^2 - y^2}$	Equation (2)
$\alpha$	Euler angle ( $\hat{\mathbf{z}}$ rotation)	Appendix C.1
$\beta$	Euler angle ( $\hat{\mathbf{y}}$ rotation)	Appendix C.1
$\gamma$	Euler angle ( $\hat{\mathbf{z}}$ rotation)	Appendix C.1
$\Gamma$	Gamma function	
$\theta$	Spherical harmonic polar angle	Equation (1)
$\theta$	Rotation angle	Appendix C.2
$\Theta$	Heaviside step function	Equation (D22)
$\lambda$	Angular position of occultor/occulted intersection point	Equation (26)
$\Lambda$	Mandel & Agol (2002) function	Equation (D22)
$\mu$	$l - m$	Equation (8)
$\mu$	Limb darkening radial parameter	Equation (37)
$\nu$	$l + m$	Equation (8)
$\Pi(\cdot, \cdot)$	Complete elliptic integral of the third kind	Equation (D24)
$\phi$	Spherical harmonic azimuthal angle	Equation (1)
$\phi$	Angular position of occultor/occulted intersection point	Equation (25)
$\varphi$	Dummy integration variable	
$\omega$	Angular position of occultor	Equation (24)